ICASE

ON THE NONLINEAR STABILITY OF A HIGH-SPEED, AXISYMMETRIC BOUNDARY LAYER

C. David Pruett
Lian L. Ng
Gordon Erlebacher

NASA

National Aeronautics and
Space Administration

Langley Research Center
Hampton, Virginia 23665-5225

ON THE NONLINEAR STABILITY
OF A HIGH-SPEED, AXISYMMETRIC BOUNDARY LAYER

C. David Pruett
National Research Council Associate

Lian L. Ng
Analytical Services and Materials

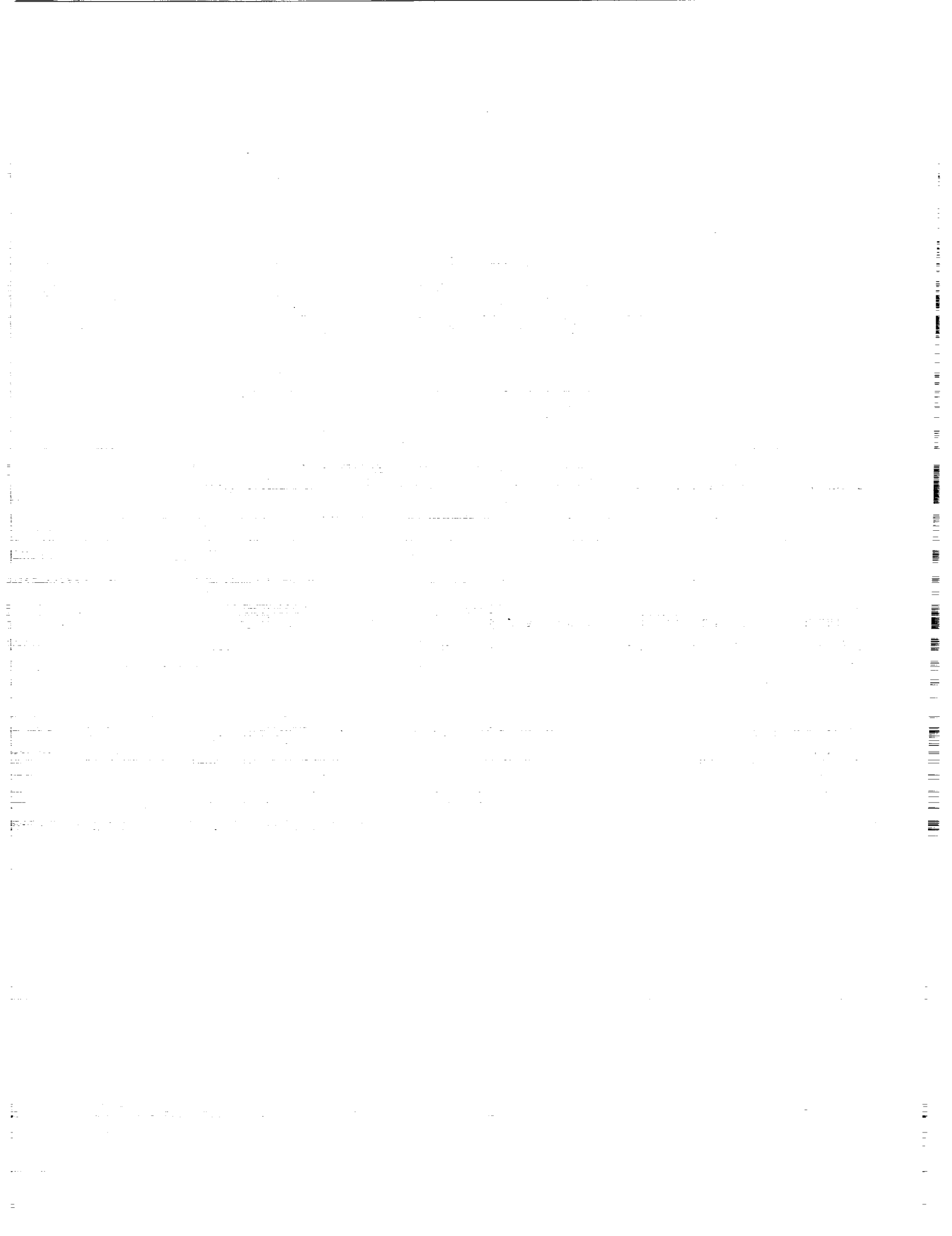Gordon Erlebacher †
Senior Scientist, ICASE

*NASA Langley Research Center
Hampton, Virginia 23665*

ABSTRACT

The stability of a high-speed, axisymmetric boundary layer is investigated using secondary instability theory and direct numerical simulation. Parametric studies based on temporal secondary instability theory identify subharmonic secondary instability as a likely path to transition on a cylinder at Mach 4.5. The theoretical predictions are validated by direct numerical simulation of temporally-evolving primary and secondary disturbances in an axisymmetric boundary-layer flow. At small amplitudes of the secondary disturbance, predicted growth rates agree to several significant digits with values obtained from the spectrally-accurate solution of the compressible Navier-Stokes equations. Qualitative agreement persists to large amplitudes of the secondary disturbance. Moderate transverse curvature is shown to significantly affect the growth rate of axisymmetric "second mode" disturbances, the likely candidates of primary instability. The influence of curvature on secondary instability is largely indirect but most probably significant, through modulation of the primary disturbance amplitude. Subharmonic secondary instability is shown to be predominantly inviscid in nature, and to account for spikes in the Reynolds stress components at or near the critical layer.

i

1. OVERVIEW

Renewed interests in the development of high-speed civil transport (HSCT) aircraft and the hypersonic National Aerospace Plane (NASP) have rekindled research in the area of high-speed transition prediction and control. With increased Mach number and higher flight altitude, the length of the transitional flow region increases, extending over large portions of aircraft surfaces. In general, realistic drag and surface heating estimates are essential to the design of high-speed aircraft and depend on accurate prediction of transition locations and extent.

In this paper, we combine secondary instability theory (SIT) with direct numerical simulation (DNS) to investigate the stability of high-speed boundary-layer flow along a prototypical "fuselage"; i.e., a cylinder. Specifically, we focus on the linear and initial nonlinear stages of forced transition, via a subharmonic secondary instability route. We find secondary instability theory and direct numerical simulation to complement one another in several ways. First, in the absence of high-speed experimental data, DNS provides a means to substantiate theory and to establish the limits of its validity. Second, within its region of validity, secondary instability theory is preferable to computationally-intensive numerical simulation to explore the parameter space. Third, when the nonlinear stages of a controlled instability process are simulated numerically, initial conditions derived from SIT provide a "jump start", thereby reducing significantly the integration times necessary to attain highly nonlinear states.

In the next section we review some experimental and theoretical results which are relevant to instability processes on cylinders. After briefly defining the geometry, governing equations, and nondimensionalization in the third section, in Section 4 we address, in general, how transverse curvature influences instability mechansims. As a preface to the discussion of secondary instability theory in Section 6, we discuss relevant results from temporal linear stability theory for compressible flows in Section 5. In Section 7, results of direct numerical simulation are presented and are compared with theory. Closing observations are offered in the final section.

2. REVIEW

Whereas instability mechanisms in incompressible boundary layers have been studied extensively, research interest in the stability of compressible flows has been sporadic. Following the pioneering work of Lees and Lin [1] in 1946, there was a very active period in compressible stability research which lasted into the early 1960's. After nearly two decades of relative dormancy, interest in this area was revived in the mid 1980's when national attention was directed toward HSCT and NASP. Theoretical papers remain relatively few and experimental results are still quite rare. Although classical linear stability theory has been thoroughly validated for incompressible boundary layers (most notably [2]), the only existing confirmations of supersonic and hypersonic stability theory of which the authors are aware are those of Laufer and Vrebalovich [3] and Kendall [4]. The former experiment investigates supersonic flow over a flat plate; the latter examines supersonic and hypersonic flow over a flat plate and hypersonic flow over a cone. Although the agreement between linear theory and these experiments is imperfect, it is encouraging, given the difficulty of making accurate measurements in a high-speed flow environment. The situation is well summarized by Laufer and Vrebalovich [3] who state: "In general, the experiments confirm the basic assumptions and predictions of the existing stability theory and also suggest the desirability of improvement in the theory in certain phases of the problem". With regard to direct numerical simulation, there have been only a handful of stability simulations for compressible flows (e.g. [5]), and all of these within the past five years, as reported by Kleiser and Zang in their recent review article [6]. In general, there remains a great need for carefully conducted experiments on compressible transition, well-coordinated with theoretical analyses and direct numerical simulations.

Concerning the cylinder, it is known from the experiment of Brown, conducted in 1957 and only recently published [7], that natural transition on a cylinder in a subsonic, axial flow occurs via the now classical secondary instability route as described by Herbert and coworkers [8,9]. Brown's experiment shows explosive secondary instability emerging from axisymmetric, finite-amplitude Tollmien-Schlichting (TS) instability waves. The wavelengths in the streamwise and azimuthal directions are roughly equal and the secondary instability is of subharmonic (H) type as evidenced by a staggered arrangement of Λ-vortices. More recently, Kegelman and Mueller [10] have observed both fundamental

(K) type and subharmonic (H) type secondary instabilities in forced transition experiments on an ogive-cylinder in a low-speed flow. At low levels of forcing and in natural transition, the staggered vortex arrangement is favored, whereas at high forcing amplitudes the tendency is toward the aligned (K) arrangement. Qualitatively, this is in keeping with observations of transition in flat-plate boundary layers as reported in [6].

With regard to (spatial) stability theory for incompressible flows along cylinders, Kao and Chow [11] show curvature to have a stabilizing trend on TS instability waves, characterized by a shift of the neutral curve toward higher Reynolds numbers in the frequency-Reynolds number stability plane.

Experiments of transition in supersonic flows along cylinders are quite rare. Among these few are the ballistic range experiments of Seiff and Short [12] and Whitfield and Iannuzzi [13]. In the former experiment, remarkable shadowgraph photographs capture laminar-turbulent transition, and, in one test case, a turbulent burst. Curiously, in the latter experiment, transition data on cones are compared to data for a hollow cylinder, which the authors claim to be "equivalent to a flat plate". Our findings do not support this equivalence. There have been, however, several transition experiments on cones [4,13-18], which are particularly enlightening. Despite simplifying assumptions which neglect some effects of transverse curvature, Mack [19] obtains qualitative agreement between linear theory and an experiment by Stetson and coworkers [14] which investigates Mach 8 flow past a sharp, 7-degree half-angle cone. The frequency of the most amplified disturbance and the neutral-curve obtained analytically by Mack match closely the experimentally-observed values. However, observed and predicted growth rates differ considerably. Another experiment of particular interest is the flow visualization experiment of Fischer and Weinstein [15] on a shallow cone in a very high-speed flow (freestream Mach number of 20) in helium. Fischer and Weinstein observe transition to originate near the critical layer and to propagate inward to the body over a relatively long distance. For hypersonic flow over a cone, Kendall [4] observes in the boundary layer "well-ordered rope-like waves ..., which persist for relatively long distances and which culminate in transition". These latter two results among others suggest at least two qualitative differences between low-speed and high-speed transition mechanisms: at high speeds the transition region is relatively long; and at high-speeds transition originates near the crit-

ical layer rather than near the wall.

With regard to the theory of stability for high-speed flows along cylinders, Duck [20] shows transverse curvature to have a stabilizing influence on inviscid, axisymmetric instability modes at (edge) Mach numbers of 2.8 and 3.8. On the basis of spatial linear stability, Malik and Spall [21] show a similar tendency for axisymmetric "second-mode" disturbances at Mach 5.0. However, they also find that "first-mode" instability waves can be destabilized by increasing curvature. These results are corroborated using temporal linear stability theory by Macaraeg and Daudpota [22] and by Pruett and Streett [23].

Finally, Ng and Erlebacher [24] examine secondary instability mechanisms in compressible flat-plate boundary layers for a variety of edge Mach numbers up to 4.5 and find subharmonic secondary instability to be a likely path to transition in high-speed flow. Unlike the explosive nature of secondary instability in incompressible flow, secondary instabilities in hypersonic flows typically grow more gradually, with amplification rates only somewhat larger than that of the most unstable primary disturbance.

These experimental and theoretical findings provide a tentative basis with regard to the investigation of high-speed instability processes on cylinders to follow. First, compressible linear stability theory is applicable, at least qualitatively. Second, transverse curvature may have a non-negligible influence on stability. And third, instabilities at high speeds may differ fundamentally from those at low speeds.

3. GEOMETRY, GOVERNING EQUATIONS, AND NONDIMENSIONALIZATION

Coordinate System and Governing Equations

Consider the compressible, axial flow along a cylinder of radius R^*, as shown in Fig. 1. If (u^*, v^*, w^*) denote velocity components in the cylindrical coordinate system (x^*, θ, r^*), and ρ^* and T^* denote the fluid density and temperature, respectively, then the flow is governed by the compressible Navier-Stokes equations in cylindrical coordinates, as given in Appendix E of Thompson [25]. Throughout this discussion, dimensional quantities are denoted by superscript *. Our interest is in the

stability of the boundary layer downstream of the bow shock. Accordingly, we assume the post-shock boundary-layer edge conditions to be constant. And, for convenience, we define the wall-normal coordinate $z^* = r^* - R^*$.

Nondimensionalization

To reduce the parameter space and to gain physical insight, it is desirable to render the governing equations dimensionless. For the problem at hand, it is most convenient to scale flow quantities by their respective edge values, denoted by subscript "e", and to scale lengths by a reference length L^* to be defined shortly. The following parameters then appear in the dimensionless governing equations: M_e, the edge Mach number; Pr, the Prandtl number; Re_{L^*}, the Reynolds number based on L^*; and γ, the ratio of specific heats. Specifically, these are defined as follows:

$$ M_e = \frac{u_e^*}{a_e^*} \quad ; \quad Pr = \frac{C_p^* \mu_e^*}{\kappa_e^*} \quad ; \quad Re_{L^*} = \frac{\rho_e^* u_e^* L^*}{\mu_e^*} \quad ; \quad \gamma = \frac{C_p^*}{C_v^*} \tag{1} $$

In eqs. (1), C_p^* and C_v^* are respectively the specific heats at constant pressure and volume, and a_e^* is the speed of sound. The ratio of specific heats and the Prandtl number are assumed here to be constant with values of 1.4 and 0.7, respectively. The viscosity μ_e^* and the thermal conductivity κ_e^* are each assumed to vary with temperature according to Sutherland's law; namely,

$$ \frac{\mu^*}{\mu_e^*} = \frac{\kappa^*}{\kappa_e^*} = \frac{T^{3/2}(1+C_1)}{T+C_1} \quad ; \quad T = \frac{T^*}{T_e^*} \quad ; \quad C_1 = \frac{T_c^*}{T_e^*} \tag{2} $$

where dimensional temperatures are expressed in degrees Rankine and $T_c^*=198.6°R$.

There are several possible choices of length scale L^*. For consistency with the work of others, we use

$$ L^* = \sqrt{\frac{v_e^* x^*}{u_e^*}} \tag{3} $$

where $v_e^*=\mu_e^*/\rho_e^*$ is the kinematic viscosity. An alternate length scale is the boundary-layer

displacement thickness defined by

$$\delta^* = \int_0^\infty [1 - \frac{\rho^* u^*}{\rho_e^* u_e^*}] dz^* \tag{4a}$$

$$\delta^* (1 + \frac{\delta^*}{2R^*}) = \int_0^\infty \frac{r^*}{R^*} [1 - \frac{\rho^* u^*}{\rho_e^* u_e^*}] dz^* \tag{4b}$$

Equation (4a) is the standard definition for planar boundary layers, whereas (4b) applies to thick axisymmetric boundary layers [26]. Note that (4b) involves the solution of a quadratic equation and that, for very large radius R^*, (4b) degenerates to (4a). At Mach 4.5 and $\delta^*/R^* \doteq 0.1$, for example, equations (4a) and (4b) differ in δ^* by about 0.5%.

4. EFFECTS OF TRANSVERSE CURVATURE

Whereas the boundary layer along a flat plate is self-similar in the absence of a streamwise pressure gradient, that along a cylinder is non-similar. It can be argued that self-similarity is possible only for geometries in which there is no inherent length scale, as is the case for semi-infinite flat plates and wedges. In contrast, the cylinder has a characteristic radius R^*. As the boundary-layer displacement thickness δ^* grows in the streamwise direction while the radius remains fixed, their ratio

$$C = \frac{\delta^*}{R^*} \tag{5}$$

by which we quantify the curvature C, increases in the streamwise direction, destroying self-similarity.

Transverse curvature C affects boundary-layer stability in two ways: "directly", through the curvature terms which appear in the linearized disturbance equations when expressed in the natural cylindrical coordinate system; and "indirectly", through streamwise evolution of the non-similar mean flow. Figure 2, obtained from the spectrally-accurate boundary-layer code of Pruett and Streett [23], shows the streamwise evolution of the mean streamwise velocity and the mean temperature in the boundary layer on a cylinder in a high-speed flow. The edge Mach number is 4.5 and the edge temperature is

$110°R$ (wind tunnel conditions). Each curve of the family corresponds to a unique curvature C, or equivalently, to a unique streamwise station x^*. Thus, it is useful to think of curvature as a function of the streamwise coordinate; i.e., $C = C(x^*)$. From eqs. (3) and (5) we obtain

$$C = \frac{1}{\sqrt{Re_{R^*}}} \sqrt{\frac{x^*}{R^*}} \frac{\delta^*}{L^*} \tag{6}$$

where

$$Re_{R^*} = \frac{\rho_e^* u_e^* R^*}{\mu_e^*} \tag{7}$$

From eq. (6) it is clear that $C(x^*)$ depends on three dimensionless quantities: the Reynolds number based on radius; the dimensionless streamwise coordinate, also based on radius (i.e., x^*/R^*); and the ratio of length scales δ^*/L^*. Of these three quantities, the first two are free parameters, whereas, as it will become clear, the latter is not. Typically, for aerodynamic applications, $C \ll 1$. However, small C does not imply immediately that curvature effects are negligible, as will be shown.

Table I below compares the flight environments and geometric characteristics of a variety of high-speed flight vehicles. In the table, M_∞ is the cruise (freestream) Mach number, h is the cruise altitude in $ft \times 10^3$, R^*_{max} is the maximum radius of the fuselage in feet, Re_1 is the freestream unit Reynolds number at cruise conditions in units of $ft^{-1} \times 10^6$, and A is the fuselage aspect ratio based on the maximum radius; i.e., $A = l^*/R^*_{max}$, where l^* is the length of the fuselage.

Flight Environments					
Vehicle	M_∞	h	Re_1	R^*_{max}	A
F-15	1.55	37	3.54	-	-
Boeing HSCT [27]	1.7	44	3.01	~6.7	~45.
MD HSCT [28]	3.2	65-70	1.50-2.03	~8.4	~37.
NASA HSCT [29]	2.62	60-68	1.42-2.17	5.765	54.6
Reentry Cone [18]	20.1-18.2	140-40	.31-40.	1.14	11.4
NASP	>10	>100	.2-.5	~10.	>20

Table I. Flight environments of various high-speed vehicles

In general the trend for all three quantities which affect curvature is toward greater influence with increased Mach number. First, as the table shows, unit Reynolds numbers tend to decrease with the higher operational altitudes of faster vehicles. Consequently, Re_{R^*} tends to decrease with increasing Mach number. Second, high-speed vehicles tend to be slender, and large aspect ratio implies that the ratio x^*/R^* can attain large values. Third, and perhaps most significant, the relative boundary-layer displacement thickness δ^*/L^* grows as M_e^2, as shown in Fig. 3 for flow over a flat plate. (Figure 3 further shows the significant effect of T_e^* on displacement thickness by comparing results based on typical wind tunnel and flight edge temperatures.) For flow along a cylinder, the ratio δ^*/L^* is also a slow function of the curvature itself as shown in Fig. 4. Thus eq. (6) is a weakly nonlinear equation for C, given M_e, Re_{R^*}, and x^*/R^*. For a high-speed flight vehicle such as the proposed NASP, where $M_\infty \gg 1$, $Re_{R^*} = O(10^6)$, and $A \gg 1$, then $C = O(10^{-1})$ at aft fuselage stations. In the next section, primary instability growth rates will be shown to be sensitive to curvature of this order.

5. PRIMARY INSTABILITY THEORY

In this section, we consider the stability of an infinitesimally small primary disturbance superimposed on a steady, laminar, compressible mean flow. The mean velocity and temperature profiles are obtained from the numerical solution of the 2D or axisymmetric compressible boundary-layer equations by the spectrally-accurate method of [23].

Although the mean flow is in general a function of both the streamwise and wall-normal coordinates, we invoke the classical parallel flow assumption whereby the streamwise variation of the mean flow is considered negligible relative to the transverse variation, a reasonable approximation for sufficiently large Reynolds numbers and sufficiently short disturbance wavelengths. As a consequence, the primary disturbance can be written in the modal form

$$\vec{q}_1(t,x,\theta,z) = \vec{\phi}_1(z)e^{i(\alpha x + \beta R \theta - \omega t)} + c.c. \tag{8}$$

where

$$\vec{q} = [\rho, u, v, w, T]^T \qquad (9)$$

and similarly for the vector $\vec{\phi}$. In eq. (8) $\alpha = \alpha^* L^*$ and $\beta = \beta^* L^*$ are streamwise and azimuthal wavenumbers, respectively, $t = t^* L^* / u_e^*$ is dimensionless time, $\omega = \omega^* u_e^* / L^*$ is dimensionless circular frequency, $\vec{\phi}$ is a complex function which defines the structure of the disturbance in the wall-normal direction, and "c.c." denotes the complex conjugate of the preceding terms. The subscript "1" refers to "primary" instability, in contrast to "secondary" instability, denoted by subscript "2" in the next section. For clarity, when no confusion is likely to result, unsubscripted wavenumbers and frequency refer to the primary instability mechanism. To preserve the azimuthal periodicity of flow along a cylinder, the product βR must be an integer.

Two theories are commonly used to study instability mechanisms. Spatial theory assumes ω to be real, while α and β are complex. The real part of α is the streamwise wave number; the negative of the imaginary part is the spatial growth rate. In contrast, in temporal theory, α and β are taken as real while ω is complex. The real and imaginary parts of ω determine, respectively, the temporal frequency and growth rate of the wave. In temporal theory, eq. (8) defines a wave with a real total wavenumber $\bar{\alpha} = \sqrt{\alpha^2 + \beta^2}$ which propagates with complex phase velocity $\bar{c} = \omega / \bar{\alpha}$ at the angle $\lambda = \tan^{-1}(\beta/\alpha)$ to the streamwise axis. Temporal and spatial theories give equivalent results only for neutrally-stable waves. An approximate relationship between temporal and spatial theories is given by the Gaster transformation [30], which is increasingly valid as growth rates tend toward zero. In the present analysis, we consider only temporally-growing instabilities.

The formulation of the eigenvalue problem for the analysis of temporally-evolving instability waves in compressible flows is well documented in Mack [31] and its numerical solution via spectral collocation methods is described thoroughly in Macaraeg et al [32]. All results presented in this section were obtained using temporal linear stability codes which are variants of that described in [32], to which the reader is referred for further detail.

A comprehensive review of the linear stability of compressible boundary layers can be found in the works of Mack [31] and Malik [33]. For completeness, some relevant results are restated here. In brief, there are at least two fundamental ways in which instability mechanisms in incompressible and

compressible boundary layers differ. First, unstable modes in compressible wall-bounded flow may exhibit either viscous or inviscid character. Second, for high-speed compressible flow, multiple instability modes may coexist.

Neutrally-Stable Modes

Unlike the incompressible Blasius boundary layer, whose velocity profile is noninflectional, the compressible flat-plate boundary layer possesses a "generalized inflection point" defined by

$$\frac{\partial}{\partial z}(\rho_0 \frac{\partial u_0}{\partial z}) = 0 \tag{10}$$

where subscript "0" denotes time-averaged (mean) quantities. As first observed by Lees and Lin [1], the presence of a generalized inflection point is necessary, and, with additional mild restrictions, sufficient to guarantee the existence of an inviscid neutral mode. A further generalization of condition (10) to compressible flow along a cylinder can be found in Duck's recent work [20]. In addition, there exist noninflectional inviscid neutral modes. Inflectional neutral modes travel with a phase velocity equal to the velocity of the mean flow at the generalized inflection point, whereas noninflectional neutral modes travel with phase velocity equal to the edge velocity u_e^* [34]. The practical implication for finite Re_{L^*} of the existence of both noninflectional and inflectional inviscid neutral modes is that, in wall-bounded supersonic flow, unstable modes may exhibit either viscous, inviscid, or mixed character. In contrast, Tollmien-Schlichting (TS) instability modes in the incompressible flat-plate boundary layer are purely viscous in origin. Here an instability mode is considered to be inviscid in origin if its growth rate increases monotonically as Re_{L^*} increases, whereas it is considered viscous if the instability vanishes as $Re_{L^*} \to \infty$.

The "First-Mode" Instability

In some sense, the so-called "first-mode" instability is the analog in compressible flow to the TS instability in incompressible flow. For edge Mach numbers below about 1.6, the inflection point lies

close to the wall and the first-mode instability is of essentially viscous nature. As Mach number increases the viscous instability mechanism weakens and the first mode instability acquires inviscid character, as the generalized inflection point migrates further from the wall. Above about M_e=2.2 inviscid amplification rates increase dramatically with increasing M_e. For edge Mach numbers above about 3.8, the first-mode instability can be considered purely inviscid, in the sense that viscosity has only a stabilizing influence over the entire range of α. Finally, unlike TS instabilities in incompressible flow, first-mode instabilities in supersonic flow are most unstable when oblique ($\beta \neq 0$) [31].

The "Second-Mode" Instability

For high supersonic and hypersonic Mach numbers, there exist high-frequency modes of instability in addition to the "first" instability mode. The first of the so-called "higher" modes is termed the "second" mode. In the flat plate boundary layer, it first appears at about M_e=2.2 and becomes more unstable with increasing Mach number until about M_e=4.5, where it is maximally unstable. The second mode dominates the first mode somewhere in an interval of about M_e=3 to M_e=4, depending upon edge temperature and other conditions. It remains the most "dangerous" (unstable) mode for high hypersonic flow. Unlike the first mode, the second mode is most unstable when it propagates in the direction of the mean flow [31].

For the flat-plate boundary layer at M_e=4.5, the regions of instability for 2D (β=0) first and second modes are distinct, as shown in Fig. 5, adapted from Mack [31]. The first and second-mode "neutral-curves" correspond to parameter pairs (α,Re_{L^*}) for which disturbances of the form (8) are neutrally stable. Parameter values corresponding to points within (without) the neutral-curves identify exponentially growing (decaying) disturbances. The lower and upper sections of each neutral curve are commonly referred to as "branch 1" and "branch 2", respectively. The points on the upper and lower branches corresponding to the inviscid limit ($Re_{L^*} \rightarrow \infty$) identify respectively the "inflectional" and "noninflectional" inviscid neutral modes described in a previous subsection [34].

Eigenfunctions

Figures 6 compare and contrast the eigenfunctions of highly-amplified first and second-mode disturbances in high-speed flow along a cylinder. The parameters of the flow are

$$M_e = 4.5 \quad ; \quad Re_{L^*} = 989.4 \ (Re_{\delta^*} = 10000.) \quad ; \quad T_e^* = 110°R \qquad (11)$$

$$Pr = 0.7 \quad ; \quad \gamma = 1.4 \quad ; \quad C = 0.1$$

The first-mode disturbance has $\lambda=58°$ and wavenumbers $(\alpha,\beta)=(0.0495,0.0792)$. The second-mode disturbance is axisymmetric with wavenumbers $(\alpha,\beta)=(0.2276,0.0)$. It is interesting to note that the temperature and density components of the eigenfunctions strongly dominate all other components, a distinguishing characteristic of instability waves in high-speed boundary layers. For the second mode at $M_e=4.5$, the maximum amplitude of the temperature fluctuation is more than 15 times that of the streamwise velocity fluctuation. The amplitude peaks of the temperature fluctuations occur very near their respective critical layers (where phase velocity equals mean streamwise velocity), as denoted by the vertical dashed lines in Figs. 6. This suggests that the critical layer plays a special role in high-speed transition. It is also interesting to note that the vertical component of the perturbation velocity is insignificant in the first-mode case, whereas it has magnitude roughly equal to the streamwise perturbation velocity in the second-mode case. The eigenfunctions for the moderate curvature $(C=0.1)$ case shown in Figs. 6 differ only slightly from their respective flat-plate $(C=0.0)$ counterparts.

Effects of Transverse Curvature

We now address how transverse curvature affects stability, relative to the stability characteristics of flow over a flat plate. In Fig. 7, we vary α to extract a vertical "slice" through Fig. 5 at a fixed Reynolds number $Re_{L^*}=955.7$, denoted in Fig. 5 by the vertical dashed line. The solid and dashed lines of Fig. 7 contrast the results for flat-plate and cylindrical geometry $(C=0.1)$, respectively. In both cases, it is clear that, at Mach 4.5, second-mode disturbances are the most "dangerous", with growth rates five times their 2D (axisymmetric) first-mode counterparts and roughly twice that of the most

unstable oblique (helical) first modes. There is a twofold effect of transverse curvature on axisymmetric first and second modes: a stabilizing trend characterized by a suppression of the first and second-mode peaks; and a shift of the most unstable wavenumbers toward shorter wavelengths. In contrast, the oblique first mode at these conditions is destabilized by increasing curvature. These trends have been observed and previously reported by Malik and Spall [21], who use spatial stability theory.

In Figs. 8, we examine the sensitivities of the growth rates of two second-mode disturbances of fixed wavenumber to variations in the curvature C. In principal, this is analogous to forcing the boundary layer at a fixed frequency and observing the change in growth rate at a fixed station as the radius of the cylinder diminishes. As in Fig. 7, $Re_{L^*}=955.7$ and $M_e=4.5$. For $\alpha=0.20$, near the lower branch of Fig. 7 where the rate of change of the growth rate with respect to wavenumber is large, the variation in C has significant effect on the growth rate (Fig. 8a). In contrast, the effect of curvature is only moderate for $\alpha=0.22$, near the maximally unstable wavenumber (Fig. 8b). Figures 8 also show the relative contributions of the "direct" and "indirect" effects of curvature, as defined in Section 4, to the "combined" effect. To obtain the "direct" influence curve, we use a flat-plate mean flow and introduce curvature only in the linearized disturbance equations. In contrast, the "indirect" influence curve results if we account for curvature in the mean flow but not in the disturbance equations. Qualitatively, the indirect and direct effects on the second mode appear to be additive.

We close this section with a brief discussion of how temporal linear stability theory is adapted to approximately model spatially-evolving disturbances in a growing boundary layer. In temporal linear theory, a disturbance of fixed dimensional wavelength (wavenumber) is the approximate analog of a fixed-frequency disturbance in spatial theory. In Fig. 5, each ray emanating from the origin corresponds to a unique dimensional wavenumber, three of which are identified as $\alpha_l^* < \alpha_m^* < \alpha_h^*$. Points along each ray correspond to unique values of the length scale L^*, or equivalently by eq. (3), to a unique streamwise station x^*. The low-wavenumber (low-frequency) disturbance, denoted by α_l^*, can trigger only a first-mode instability, whereas the high-wavenumber disturbance, denoted by α_h^*, can give rise only to a second-mode instability. However, the disturbance of moderate wavenumber α_m^* can trigger either first or second-mode instabilities, depending upon L^*.

In a growing boundary layer, the increase in L^* associated with increasing x^* leads naturally to the growth, stabilization, and decay of disturbances of certain wavenumbers α^*. For example, in Fig. 5, point E on the lower branch (branch 1) identifies the value of x^* beyond which a small-amplitude disturbance of wavenumber α_h^* becomes unstable and begins to grow exponentially. At the value of x^* corresponding to point F on the upper branch (branch 2), the disturbance again passes through neutral stability. Further downstream the disturbance is stable and its amplitude will decay. If nonlinear effects are insignificant, the wave attains its maximum (presumably finite) amplitude at point F, and the ratio of amplitudes at points F and E is given by

$$\frac{A_F}{A_E} = e^{\int_{x_E}^{x_F} \omega_i(x)dx} \tag{12}$$

where $\omega_i(x)$ is the growth rate as a function of position x along the ray. Nonlinear saturation mechanisms may dramatically alter the scenario above if wave amplitude becomes large; however, because of the relatively low growth rates of instabilities in high-speed boundary-layer flow, linear theory is probably adequate to describe the primary instability mechanism unless the flow is forced at very high amplitudes.

Figs. 5, 7, and 8, and eq. (12), taken together, imply that moderate transverse curvature may significantly alter the long term temporal or spatial evolution of primary instability waves, particularly forced instability waves. In the next section we show the onset of secondary instability to be quite sensitive to the amplitude of the primary disturbance. Thus, curvature may exert an indirect yet significant influence on transition.

6. SECONDARY INSTABILITY THEORY (SIT)

The secondary instability theory on which the results of this section are based is a generalization to compressible flow of the work of Herbert [9]. Details can be found in the recent work of Ng and Erlebacher [24], which is summarized below.

We consider the stability with respect to small perturbations of an axisymmetric base flow comprised of a steady, parallel mean flow onto which a finite-amplitude, "neutrally-stable" primary disturbance is superimposed. Specifically, following the notation of the previous section, the base flow can be written

$$\vec{q}_b(t,x,z) = \vec{q}_0(z) + \varepsilon_1 \vec{q}_1(z)e^{i(\alpha x - \omega_1 t)} + c.c. \tag{13}$$

where subscripts "0" and "b" refer to "mean" and "base" flows respectively, and "ε_1" is the amplitude of the primary instability wave (normalized so that the maximum amplitude of the temperature fluctuation is unity). Here we consider only axisymmetric primary waves, although in the more general theory [24], the primary wave can be oblique (helical). Again we restrict consideration to the temporal model of stability in which the wavenumber α is real. In a frame of reference $x' = x - c_1 t$ which moves with the phase velocity $c_1 = \mathrm{Re}(\omega_1/\alpha)$ of the primary wave, the base flow is independent of time and periodic in the streamwise spatial dimension. Consequently, the stability analysis is amenable to Floquet theory [9], which applies to differential equations with periodic coefficients. With guidance from Floquet theory, a general *ansatz* for a secondary disturbance ensemble of N wave components is as follows:

$$\vec{q}_2(t,x,\theta,z) = e^{-i\omega_2 t}e^{ih\frac{\alpha}{2}x'}e^{i\beta R\theta}\sum_{j=-N/2}^{N/2-1}\vec{\phi}_{2,j}(z)e^{ij\alpha x'} + c.c. \quad (N \; even) \tag{14a}$$

$$\vec{q}_2(t,x,\theta,z) = e^{-i\omega_2 t}e^{ih\frac{\alpha}{2}x'}e^{i\beta R\theta}\sum_{j=-(N-1)/2}^{(N-1)/2}\vec{\phi}_{2,j}(z)e^{ij\alpha x'} + c.c. \quad (N \; odd) \tag{14b}$$

where eqs. (14a) and (14b) are valid for an even and odd number of wave components respectively. In eqs. (14), subscript "2" denotes "secondary" disturbance, and h is the "detuning parameter". Henceforth, β without subscripts refers to the azimuthal wavenumber of the secondary disturbance. For $h=1$, the secondary disturbance is of subharmonic (H) type, whereas for $h=0$ it is of fundamental (K) type. For $0 < h < 1$, eqs. (14) model so-called "detuned" secondary instability modes. In practice, the parameters of the neutrally-stable primary wave correspond to some point along the upper branch of the neutral-stability curve, in keeping with the discussion of Fig. 5 in the previous section.

Let us now choose wavenumbers α and β and suppose $\vec{q} = \vec{q}_b + \varepsilon_2 \vec{q}_2$, where $\vec{q}_b$ and $\vec{q}_2$ are defined in eqs. (13) and (14), respectively, and where ε_2 is the amplitude of the secondary disturbance, presumed small. Substitution of $\vec{q}$ into the compressible Navier-Stokes equations, neglect of nonlinear terms in ε_1^2 and ε_2^2, and discretization in the z direction, results in a complex generalized eigenvalue problem for the eigenvalue ω_2 and the discrete eigenvector $\vec{\phi}_2 = [\vec{\phi}_{2,0}, \vec{\phi}_{2,-1}, \vec{\phi}_{2,1}, ...]^T$, namely

$$(A_3 D^2 + A_2 D^1 + A_1)\vec{\phi}_2 = \omega_2 A_0 \vec{\phi}_2 \tag{15}$$

In eq. (15), D^p denotes a p-fold discrete spatial differentiation operator, and the A_i's are complex matrices of dimension $5MN \times 5MN$, where M is the number of discrete grid points in z. The nearly one thousand lines of FORTRAN code required to evaluate the coefficients of the A_i matrices are generated with the help of MACSYMA, a symbolic manipulation language, without which the analysis of compressible secondary instability would be a formidable task. Even with a highly-accurate numerical method, such as the spectral collocation method in current use, in which typically $M=73$, the memory requirement for an eigenvalue calculation of $N>6$ becomes prohibitively large. Fortunately, only a very few components of (14) are of major importance, as suggested in Table II.

Eigenvalue vs. Number of Components		
N	$Im(\omega_2)$	$-Re(\omega_2)$
2	0.002416	$<10^{-5}$
3	0.002411	$<10^{-5}$
4	0.002406	$<10^{-5}$

Table II. Variation of the Eigenvalue of a Subharmonic Secondary Instability with Number of Components N.

The results presented in Table II are for subharmonic ($h=1$) secondary instability. The flow parameters are the same as in eqs. (11). The primary disturbance is an axisymmetric second mode of wavenumber $\alpha=0.2523$, amplitude $\varepsilon_1=.085$, and frequency $\omega_1 = 0.2275 + i0.436 \times 10^{-4}$. The azimuthal wavenumber of the secondary disturbance is $\beta=0.2673$. Due to memory limitations and contamination by round-off error, it is not computationally feasible to include enough components in the eigenvalue problem to

demonstrate convergence of the *ansatz* (14) in a rigorous mathematical sense. Rather, we have verified the eigenvalues by comparison against spectrally-accurate direct numerical simulation. With the inclusion of just two (N=2) wave components in the secondary disturbance, the eigenvalue is correct to two significant digits. That Re(ω_2) is essentially zero in the frame x' implies that the primary and secondary disturbances are phase locked.

Figure 9 displays a rather typical scenario for secondary instabilities at subsonic and low supersonic Mach numbers. The parameter values for this test case, in which four components (N=4) have been retained in the *ansatz* (14), are

$$M_e = 1.6 \quad ; \quad Re_{L^*} = 613.2 \ (Re_{\delta^*} = 1641) \quad ; \quad T_e^* = 520°R \qquad (16)$$

$$\alpha = 0.0867 \quad ; \quad \beta = 0.1336 \quad ; \quad C = 0.051$$

The subharmonic secondary instability mechanism is favored at low to moderate amplitudes of the primary disturbance, whereas the fundamental secondary instability is more unstable at higher primary amplitudes. This suggests that subharmonic instability is more "dangerous" in natural transition in this speed range, in keeping with experimental observations for low-speed flow. At higher Mach numbers, there is some evidence that subharmonic secondary instability is yet more strongly favored. Figure 10 displays the growth rate of the secondary instability as a function of the detuning parameter h for a fixed, moderate-amplitude (ϵ_1=0.085) primary disturbance. The parameter values of the flow are the same as those in eqs. (11) except that Re_{L^*}=994.6. The disturbance parameters are α=0.2506, βR=21, and N=2. Of all possible secondary instabilities, the subharmonic type (h=1) is most unstable. Moreover, no fundamental type instability exists for these parameter values. Consequently, we consider henceforth only secondary instabilities of subharmonic type.

The nature of secondary instability is that it is triggered only after the primary has achieved some threshold amplitude. This is clearly shown in Fig. 11 which presents the growth rate of a subharmonic secondary disturbance of N=2 vs. primary wave amplitude ϵ_1. Again, the flow parameters are the same as given in eqs. (11), except that Re_{L^*}=955.7. In this case, the disturbance parameters are α=0.2400

and β=0.2000. For $\epsilon_1 < 2.5\%$, no secondary instability is present. For $\epsilon_1 > 2.5\%$, secondary instabilities exist which, at large ϵ_1, attain growth rates slightly higher than that of the maximally unstable second-mode disturbance at the same Re_{L^*}. Figure 11 also compares the results for the flat plate with those of a cylinder of curvature C=0.1. It appears that secondary instabilities *per se* are little affected by moderate transverse curvature. This is further substantiated in Fig. 12, which shows only slight influence of transverse curvature on the growth rate of the secondary instability, for a fixed 8.5% primary disturbance amplitude. However, since the growth rate of the secondary disturbance is strongly dependent on primary disturbance amplitude, which is itself sensitive to curvature effects (refer to Fig. 5, eq. (12), and Fig. 11), the indirect influence of curvature on secondary instability may be substantial. Except for the variation in C and the fixed ϵ_1, the parameter values for Fig. 12 are the same as those for Fig. 11.

It is interesting to compare the eigenfunctions of primary (Figs. 6) and secondary disturbances, the latter shown in Fig. 13. Here, the parameter values are the same as those given for Table II, with N=2 and ϵ_1=0.085. Like the eigenfunction of the primary disturbance, the eigenfunction of the secondary disturbance is dominated by the temperature component which peaks in amplitude near the critical layer (z^*=1.08δ^*). However, unlike the primary mode, the secondary eigenfunction has very little structure near the wall. Remarkably, the structure of the eigenfunction of the subharmonic secondary disturbance is qualitatively very similar to that of a helical first-mode disturbance (Fig. 6a).

The amplitude of the secondary disturbance eigenfunction, peaked well away from the wall, its relative insensitivity to changes in the mean flow (refer to Fig. 12), and its relatively large growth rate, suggest that the secondary instability mechanism is predominantly inviscid. This suspicion is confirmed by Fig. 14. For a fixed primary disturbance with Re_{L^*}=955.7, α=0.2400, and ϵ_1=0.085, the Reynolds number of the eigensystem for a secondary disturbance of β=0.2000 and N=2 is allowed to vary artificially from about 10^3 to 1.5×10^6, while all other parameters remain fixed. The growth rate of the secondary mode increases monotonically with increasing Re_{L^*} and asymptotes at large Re_{L^*} to approximate values of 0.0053 for C=0.0 and 0.0052 for C=0.1. The figure confirms once again, that for fixed primary disturbance amplitude, the secondary instability mechanism is minimally influenced by

moderate transverse curvature.

7. DIRECT NUMERICAL SIMULATION (DNS)

The 3D, compressible Navier-Stokes equations in primitive variables $[\rho, u, v, w, p]$ (where p is the pressure) are solved by a highly-accurate spectral collocation method developed to numerically study instabilities in the flat-plate boundary layer [5]. The algorithm, adapted to the cylindrical (x, θ, z)-coordinate system of Fig. 1, treats either flat-plate or cylindrical geometry, depending on the value of a switch parameter. A temporal model of stability is assumed, in keeping with the linear analyses of primary and secondary instabilities presented earlier. As before, the mean flow is regarded as locally parallel and subject to temporally-evolving, spatially-periodic perturbations. Since the parallel mean flow does not exactly satisfy the viscous Navier-Stokes equations, small forcing terms are added to the governing equations sufficient to suppress temporal evolution of the mean flow. The spectral collocation method employs Fourier basis functions in the periodic streamwise-x and azimuthal-θ directions, and Chebyshev polynomial basis functions in the aperiodic wall-normal-z direction. Stretching and clustering mappings in the (finite) wall-normal direction concentrate collocation points in regions of severe gradients; i.e., at the wall and at the critical layer. These mappings are detailed in [5].

The governing equations and boundary conditions define an initial value problem which is integrated in time explicitly, by means of a 3rd-order, low-storage, Runge-Kutta scheme [35]. Initial conditions are formed by superposition of a parallel mean flow, derived from a spectrally-accurate boundary-layer code [23], and eigenfunctions of primary and secondary disturbances, generated from the temporal stability code of [24], also spectrally accurate. The mean boundary-layer profiles are generated assuming an adiabatic wall. In the direct simulation, the temperature at the wall is kept fixed at its mean value, and no-slip conditions are imposed on the velocity components. Either Dirichlet or Neumann conditions are enforced at the far-field boundary, with little effect on the solution provided the boundary is at sufficiently large z. The values of density at the wall and at the far-field boundary are obtained by projecting forward in time using the Runge-Kutta integrator. Pressure at the wall is extracted from the equation of state.

Test Case

The parameters of the test case are as follows:

$$M_e = 4.5 \quad ; \quad Re_{L^*} = 994.6 \quad ; \quad T_e^* = 110°R \qquad (17)$$

$$Pr = 0.7 \quad ; \quad \gamma = 1.4 \quad ; \quad C = 0.1$$

The Mach 4.5 case at a typical wind-tunnel edge temperature was selected for several reasons. As mentioned previously, the second mode is most unstable at Mach 4.5 so that the most likely type of primary instability is well-defined. Furthermore, this case has been investigated previously for flow over a flat plate by Mack [31], using linear stability theory, and by Erlebacher and Hussaini [5], using direct numerical simulation. Thus, there is data against which to compare the results for cylindrical flow. Finally, we assume a moderate degree of curvature ($C=0.1$), large enough to influence stability, yet within the range of values encountered in high-speed flight.

Initial Conditions

The wavenumbers, amplitudes, and eigenvalues of the instability waves imposed initially are given in Table III below.

Initial Conditions				
Instability	α	β	ω	ε
Primary (1,0)	0.2506	0.0	0.2261 + 0.00032i	0.0850
Secondary (1/2,±1)	0.1253	±0.2079	0.2261 + 0.00253i	0.0085
Secondary (3/2,±1)	0.3759	±0.2079	0.2261 + 0.00253i	0.0085

Table III. Disturbance initial conditions

For simplicity, we adopt a modal notation whereby "(i,j)" refers to a wave of wavenumbers $(i\alpha, j\beta)$. The primary (1,0) wave is an axisymmetric second mode of nearly neutral stability, whose parameters correspond to a point near the upper branch of the second-mode neutral curve. The secondary distur-

bance, obtained in the manner of the previous section, is of subharmonic type with $\beta R = 21$ and $N = 4$. The (1/2,1) component of the secondary wave ensemble has $\lambda = 60°$. For this value of λ, the secondary disturbance is very nearly maximally unstable with respect to β. The initial amplitude ε_2 of the secondary wave ensemble is ten times smaller than that of the primary wave, based on the relative peak amplitudes of the temperature fluctuations of the (1,0) and (1/2,1) waves.

Results

The results shown here are for a simulation of 12×12×65 resolution with equally-spaced points in the periodic dimensions and with the near-wall collocation points in the wall-normal direction distributed as shown by the symbols in Fig. 16. The bounds of the computational domain are

$$0 \le x \le \frac{4\pi}{\alpha}$$
$$0 \le \theta \le \frac{2\pi}{\beta R} \tag{18}$$
$$0 \le \frac{z^*}{\delta^*} \le 15$$

The fully-explicit time advancement results in a severe constraint on the time step when used in conjunction with the Chebyshev spectral collocation method. About 8000 time steps per period of oscillation of the primary are required to maintain numerical stability. The simulation requires about 38 minutes of CPU time on a Cray Y-MP per period of oscillation. Resolution (decay of the spectral coefficients) was monitored throughout the computation, which was halted at about 38 periods (24 CPU hours) when resolution began to deteriorate rapidly. Work is in progress to continue the simulation further into the nonlinear regime using a refined mesh and a high-order compact-differencing scheme in the wall-normal direction.

Fig. 15 shows the temporal evolution of the "energy" in various harmonics of the primary and secondary disturbances, based on a Fourier decomposition in the periodic dimensions and an integrated average in the wall-normal dimension; namely,

$$E_{ij} = \frac{1}{2}\frac{L^*}{\delta^*}\int_0^{z_{max}} \rho_0[|U_{ij}|^2 + |V_{ij}|^2 + |W_{ij}|^2]\frac{r}{R}dz \qquad (19)$$

where upper case U_{ij} represents the (i,j)-th complex Fourier component of the streamwise velocity, etc. Solid and dashed lines show results of the simulation whereas circles denote the predicted values based on linear theory for primary and secondary instabilities. The growth rate of the primary (1,0) wave is in close agreement with theory for more than 30 periods of oscillation. Initially, the (1/2,1) and (1/2,-1) (coincident) components of the secondary disturbance grow at a rate which agrees to several significant digits with the values predicted by secondary instability theory. These modes begin to depart toward slightly higher growth rates at around 10-15 periods of oscillation of the primary. Over the lengthy integration, the slightly non-neutral primary increases in amplitude by a factor of about 1.5 as shown in Fig. 16. The squares in Fig. 15 denote adjustments to the theory to incorporate the gradual increase in amplitude of the primary, and are obtained by integrating the following set of ordinary differential equations for the primary and secondary amplitudes A_1 and A_2, respectively:

$$\frac{dA_1}{dt} = \text{Im}(\omega_1)A_1 \qquad (20)$$

$$\frac{dA_2}{dt} = \text{Im}(\omega_2(A_1))A_2$$

In eqs. (20), $\text{Im}(\omega_1)$ is assumed constant, but $\text{Im}(\omega_2(A_1))$ is interpolated from the data in Fig. 11. This correction slightly overpredicts the upward deflection in the growth of the (1/2,1) mode. In contrast, the (3/2,1) and (coincident) (3/2,-1) components of the secondary disturbance grow consistently at the rate $\text{Im}(\omega_1 + \omega_2)$, denoted by triangles in Fig. 15. This is precisely the rate one would anticipate based on a weak quadratic nonlinear interaction between the primary (1,0) wave and secondary (1/2,1) wave.

Qualitative agreement between theory and simulation persists until about period 35, when the growth rate of the primary disturbance deviates significantly from the value predicted by linear theory. At this stage, modes generated by nonlinear interactions are attaining significant energies, and transition appears to be imminent. In particular, the (1,2) mode, which originates from the self-interaction of the (1/2,1) wave, has an energy content nearly equal to that of the primary instability wave. By the time

the computation is terminated at period 37.7, the temperature component of the secondary (1/2,1) wave has grown to more than 15 times its initial amplitude, as shown in Fig. 17.

Reynolds Stresses

Figure 18, obtained from the results of DNS, presents the four significant components of the six possible Reynolds stress components. These are computed in temporal theory according to

$$\tau_{i,j}(z,t) = \frac{\iint \rho_0 u_i' u_j' r d\theta dx}{\iint r d\theta dx} \tag{21}$$

where primes denote perturbation variables; e.g., $u' = u - u_0$. The individual curves in the four plots represent the wall-normal distribution of Reynolds stress at intervals of 6 periods in time, beginning with the initial condition and ending at period 36. With the exception of the $\tau_{z,z}$ component, all Reynolds stress components are peaked at the critical layer, denoted by dashed lines. In Fig. 19, we examine the relative contributions of the primary and secondary disturbances to the $\tau_{x,z}$ component. It is clear that the large growth in Reynolds stress at the critical layer is due almost entirely to the secondary instability mechanism. Fig. 19 further compares the results of SIT and DNS with regard to $\tau_{x,z}$. Theory and simulation can be considered in qualitative agreement to about period 18. Beyond that, there is gradual broadening of the stress peak in the DNS results, due presumably to nonlinear effects.

In Fig. 20 we make use of the Gaster transformation [30], based on the phase speed $c_1 = Re(\omega_1)/\alpha$ of the primary wave, to convert the temporal evolution of $\tau_{x,z}$ to an approximate spatial distribution. For clarity in Fig. 20, intervals between tick marks along the streamwise x axis are 10 displacement thicknesses in length whereas intervals in the radial direction each denote a single displacement thickness. Moreover, it should be noted that the contour intervals are different for Reynolds stress levels below and above 0.04×10^{-4}. It is interesting to view Figs. 19 and 20 in light of the high-speed experiment of Fischer and Weinstein [15], in which transition is observed to originate near the critical layer and to propagate inwardly to the body. These figures suggest a similar evolution to transition and a possible link between secondary instability theory and observed phenomena.

The initial and final times of the temporal simulation correspond via the Gaster transformation [30] to approximate initial and final streamwise stations of $x_0^* = 10R^*$ and $x_1^* = 19R^*$ respectively. Over this spatial extent, the boundary layer would have thickened by about 35%, a change of length scale large enough to significantly alter the growth of the primary disturbance according to Fig. 5. It appears that modeling the growth of the boundary-layer is a necessity if direct simulation of high-speed transition is to be quantitatively valid. Within the context of temporal DNS, this can be approximated through time evolution of the mean flow. Alternately, one must resort to more computationally-intensive spatial DNS.

Fluid Rotation

It has been suggested by Morkovin [34], that the "angular momenta" vector $\rho\vec{\omega}$ is more physically meaningful for compressible flows than is the vorticity vector $\vec{\omega} = \nabla \times \vec{u}$. This can be inferred as well from the presence of density in the generalized inflection point condition (10). In Figs. 21 we compare contours of azimuthal vorticity $\omega_\theta = \dfrac{L^*}{\delta^*}\left(\dfrac{\partial u}{\partial z} - \dfrac{\partial w}{\partial x}\right)$ with contours of azimuthal angular momentum $\rho\omega_\theta$ at period 37.7 of the numerical simulation. The contour patterns are quite different, due in part to the decreased mean density at the wall. Particularly in Fig. 21b, it is clear that a highly rotational layer has formed at the critical layer, with rotational peaks at intervals of the subharmonic wavelength $4\pi/\alpha$.

8. CONCLUSIONS

Because of the computational expense of direct numerical simulation, our work to date has been restricted to very few parameter sets and is very much "in progress". Accordingly, these comments should perhaps be interpreted as "observations" rather than as "conclusions".

1) Secondary instability of subharmonic type exists in high-speed boundary-layer flows over flat plates and cylinders, and is a likely path to transition. However, due to a general stabilizing trend with increasing M_e, secondary instabilities at high-speeds are not as "explosive" as their counter-

parts in incompressible flow. The regions of linear and nonlinear growth are relatively long, and the boundary layer may experience significant growth during laminar-turbulent transition. Growth of the boundary layer needs to be modeled if the results of direct numerical simulation are to be quantitatively valid.

2) For primary and secondary instability mechanisms, the temperature and density components of the eigenfunctions dominate at high-speeds. For example, at Mach 4.5, axisymmetric second-mode disturbances exhibit peak temperature-fluctuation amplitudes which are 15 times that of stream-wise velocity fluctuations.

3) For primary and secondary instabilities, the peak amplitudes of the temperature fluctuations occur at or very near the critical layer. Thus, the critical layer plays an important role in the instability mechanisms which arise in high-speed, wall-bounded flows.

4) The principal effect of transverse curvature on primary and secondary instability mechanisms seems to be quantitative rather than qualitative. In general, axisymmetric primary instability modes are stabilized by moderate curvature, which in turn should delay the onset of secondary instability. Curvature effects tend to become more significant with decreasing Reynolds number and increasing Mach number.

5) The amplitude of the eigenfunction of a secondary disturbance, with little structure at the wall; the relative insensitivity of secondary disturbances to changes in the mean flow; the relatively large growth rates of secondary instabilities; and the persistence of the secondary instability mechanism as $Re_{L^*} \rightarrow \infty$, all suggest that the secondary instability mechanism is predominantly inviscid.

6) In high-speed boundary-layer flow, secondary instability is responsible for large Reynolds stresses near the critical layer, and offers a possible explanation for the phenomenon observed experimentally by Fischer and Weinstein [15]. Moreover, insight gained from secondary instability theory may provide a means to refine transition models based on Reynolds stresses.

7) Secondary instability theory offers a possible means of refining the e^N method for transition prediction, based on a primary disturbance amplitude criterion rather than on an amplitude-ratio criterion.

We conclude by reiterating that there is great need for carefully-conducted compressible stability experiments, well-coordinated with analyses and direct numerical simulation.

ACKNOWLEDGMENTS

REFERENCES

1) Lees, L., and C. C. Lin, "Investigation of the Stability of the Laminar Boundary Layer in Compressible Fluid", *NACA TN-1115*, 1946.

2) Schubauer, G. B., and H. K. Skramstad, "Laminar Boundary Layer Oscillations and Stability of Laminar Flow", *J. Aeronaut. Sci.*, Vol. 14, pp. 69-78, 1947.

3) Laufer, J., and T. Vrebalovich, "Stability and Transition of a Supersonic Laminar Boundary Layer on an Insulated Flat Plate", *J. Fluid Mech.*, Vol. 9, pp. 257-299, 1960.

4) Kendall, J. M., Jr., "Wind Tunnel Experiments Relating to Supersonic and Hypersonic Boundary-Layer Transition", *AIAA J.*, Vol. 13, No. 3, pp. 290-299, 1975.

5) Erlebacher, G., and M. Y. Hussaini, "Numerical Experiments in Supersonic Boundary-Layer Stability", *Phys. Fluids A*, Vol. 2, No. 1, pp. 94-104, 1989.

6) Kleiser, L., and T. A. Zang, "Numerical Simulation of Transition in Wall-Bounded Shear Flows", to appear *Ann. Rev. Fluid Mech.*, Vol. 23, 1991.

7) Mueller, T. J., "The Role of Smoke Visualization and Hot-Wire Anemometry in the Study of Transition", *Recent Advances in Turbulence*, edited by R. E. A. Arndt and W. K. George, Hemisphere Press, Washington, 1987.

8) Herbert, T., "Secondary Instability of Boundary Layers", *Ann. Rev. Fluid Mech.*, Vol. 20, pp. 487-526, 1988.

9) Herbert, T., F. Bertolotti, and G. Santos, "Floquet Analysis of Secondary Instabilities in Shear Flows", *Instability of Time Dependent and Spatially Varying Flows*, edited by D. L. Dwoyer and M. Y. Hussaini, Springer-Verlag, pp. 43-57, 1985.

10) Kegelman, J. T., and T. J. Mueller, "Experimental Studies of Spontaneous and Forced Transition on an Axisymmetric Body", *AIAA Paper 84-0008*, presented at AIAA 22nd Aerospace Sciences Meeting, Reno, Nevada, January 9-12, 1984.

11) Kao, K.-H., and C.-Y. Chow, "Stability Analyses of Boundary Layer on a Semi-Infinite Circular Cylinder With and Without Spin", *AIAA Paper 90-0116*, presented at 28th Aerospace Sciences Meeting, Reno, Nevada, January 8-11, 1990 .

12) Seiff, A., and B. J. Short, "An Investigation of Supersonic Turbulent Boundary Layers on Slender Bodies of Revolution in Free Flight by Use of a Mach-Zehnder Interferometer and Shadowgraphs", *NACA TN-4364*, 1958.

13) Whitfield, J. D., and F. A. Iannuzzi, "Experiments on Roughness Effects on Cone Boundary-Layer Transition Up to Mach 16", *AIAA J.*, Vol. 7, No. 3, pp. 465-470, 1969.

14) Stetson, K. F., Thompson, E. R., Donaldson, J. C., and Siler, L. G., "Laminar Boundary Layer Stability Experiments on a Cone at Mach 8, Part 1: Sharp Cone", *AIAA Paper 83-1761*, July 1983.

15) Fischer, M. C., and L. M. Weinstein, "Cone Transitional Boundary-Layer Structure at $M_e=14$", *AIAA J.*, Vol. 10, No. 5, pp. 669-701, 1972.

16) Ericsson, L. E., "Effect of Nose Bluntness and Cone Angle on Slender-Vehicle Transition", *AIAA J.*, Vol. 26, No. 10, pp. 1168-1174, 1988.

17) Pate, S. R., "Measurements and Correlations of Transition Reynolds Numbers on Sharp Slender Cones at High Speeds", *AIAA J.*, Vol. 9, No. 6, pp. 1082-1089, 1971.

18) Wright, R. L., and E. V. Zoby, "Flight Boundary Layer Transition Measurements on a Slender Cone at Mach 20", *AIAA Paper 77-719* presented at 10th AIAA Fluid and Plasma Dynamics Conference, Albuquerque, New Mexico, June 27-29, 1977.

19) Mack, L. M., "Stability of Axisymmetric Boundary Layers on Sharp Cones at Hypersonic Mach Numbers", *AIAA Paper 87-1413*, presented at AIAA 19th Fluid Dynamics, Plasma Dynamics and Lasers Conference, Honolulu, Hawaii, June 8-10, 1987.

20) Duck, P. W., "The Inviscid Axisymmetric Stability of the Supersonic Flow Along a Cylinder", *J. Fluid Mech.*, Vol. 214, pp. 611-637, 1990.

21) Malik, M. R., and R. E. Spall, "On the Stability of Compressible Flow Past Axisymmetric Bodies", *High Technology Report No. HTC-8905*, Hampton, Virginia, October 1989.

22) Macaraeg, M. G., and Q. I. Daudpota, "Numerical Studies of Transverse Curvature Effects on Compressible Flow Stability", submitted to *Phys. Fluids.*

23) Pruett, C. D., and C. L. Streett, "A Spectral Collocation Method for Compressible, Nonsimilar Boundary Layers", submitted to *Int. J. Num. Meth. Fluids.*

24) Ng, L., and G. Erlebacher, "Secondary Instabilities in Compressible Boundary Layers", *ICASE Report No. 90-58 (NASA Contractor Report 182091)*, 1990.

25) Thompson, P. A., *Compressible Fluid Dynamics*, McGraw-Hill, 1972, pp. 632-635.

26) White, F. M., *Viscous Fluid Flow*, McGraw-Hill, 1974, pp. 347-350.

27) Vachal, J., "Phase IIIa Technical Review--Environmental Studies and Innovative Concepts", NASA High-Speed Civil Transport Studies, The Boeing Company, Oct. 5, 1989.

28) "Phase IIIa High Speed Civil Transport Status Review" (NASA Contract NAS1-18378), McDonnell Douglas Corporation, Oct. 5, 1989.

29) Fetterman, D. E., Jr., "Preliminary Sizing and Performance of Aircraft", *NASA TM-86357*, July 1985.

30) Gaster, M., "A Note on the Relation between Temporally-Increasing and Spatially-Increasing Disturbances in Hydrodynamic Stability", *J. Fluid Mech.*, Vol. 14, pp. 222-224, 1962.

31) Mack, L. M., "Boundary-Layer Linear Stability Theory", *Special Course on Stability and Transition of Laminar Flow*, edited by R. Michel, AGARD Report No. 709, pp. 3-1,3-81, 1984. 1990.

32) Macaraeg, M. G., C. L. Streett, and M. Y. Hussaini, "A Spectral Collocation Solution to the Compressible Stability Eigenvalue Problem", *NASA TP-2858*, 1988.

33) Malik, M. R., "Prediction and Control of Transition in Supersonic and Hypersonic Boundary Layers", *AIAA J.*, Vol. 27, No. 11, 1989.

34) Morkovin, M. V., "Transition at Hypersonic Speeds", *ICASE Interim Report 1 (NASA Contractor Report 178315)*, May 1987.

35) Williamson, J. H., "Low-Storage Runge-Kutta Schemes", *J. Comp. Phys.*, Vol. 35, pp. 48-56, 1980.
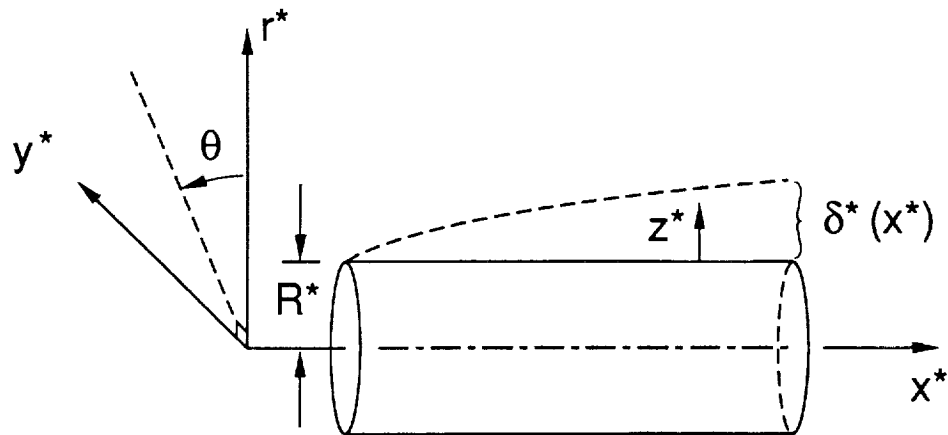
1)   Cylindrical coordinate system.

Mean Flow Profiles in the Boundary Layer along a Cylinder

$M_e = 4.5 \quad T_e^* = 110 \ R$
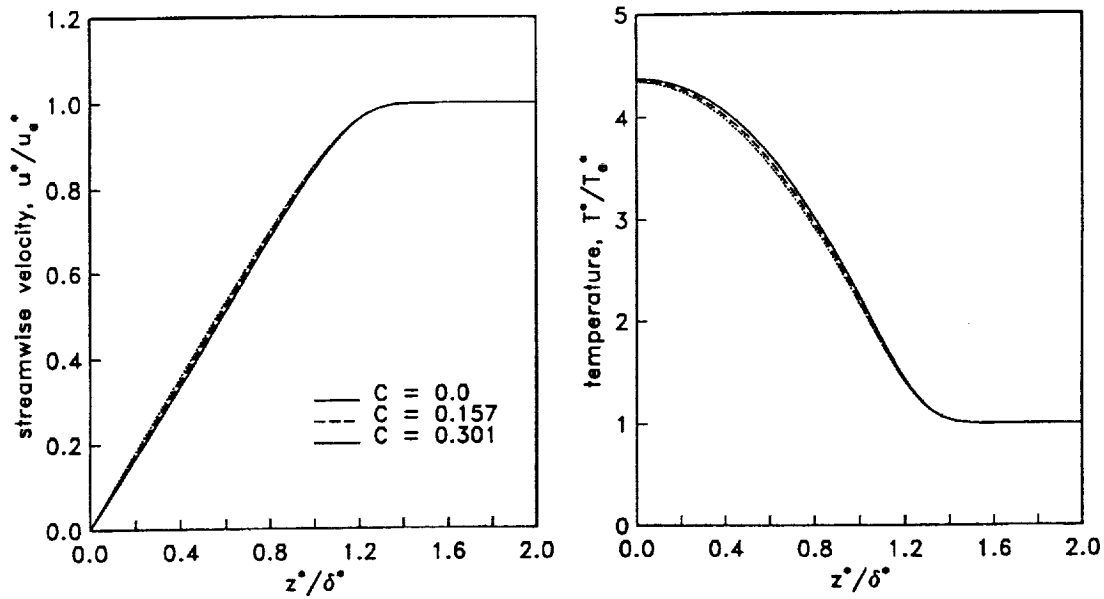
2)   Streamwise evolution of mean streamwise velocity and mean temperature in the boundary layer of a cylinder.

## Growth of Displacement Thickness with Mach No.
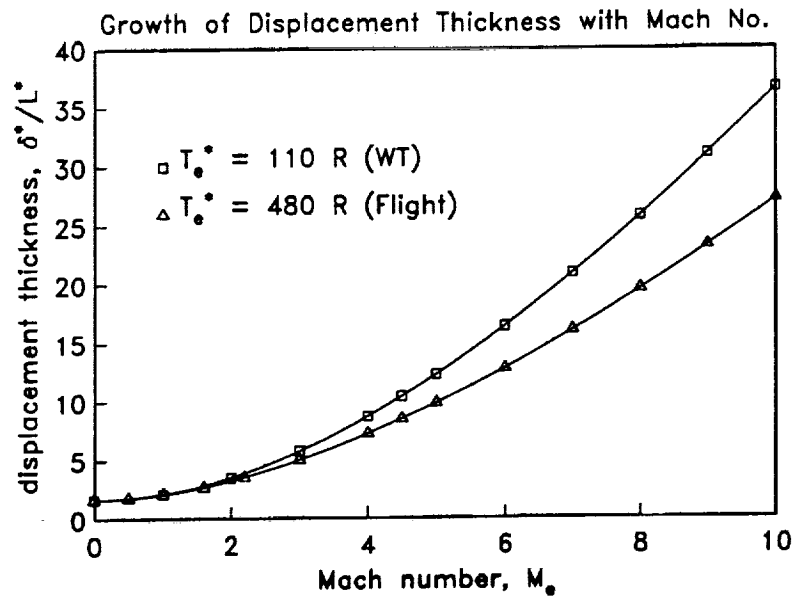
3) Growth with increasing Mach number of relative boundary-layer displacement thickness δ^*/L^* on a flat plate.

Normalized Displacement Thickness vs. C
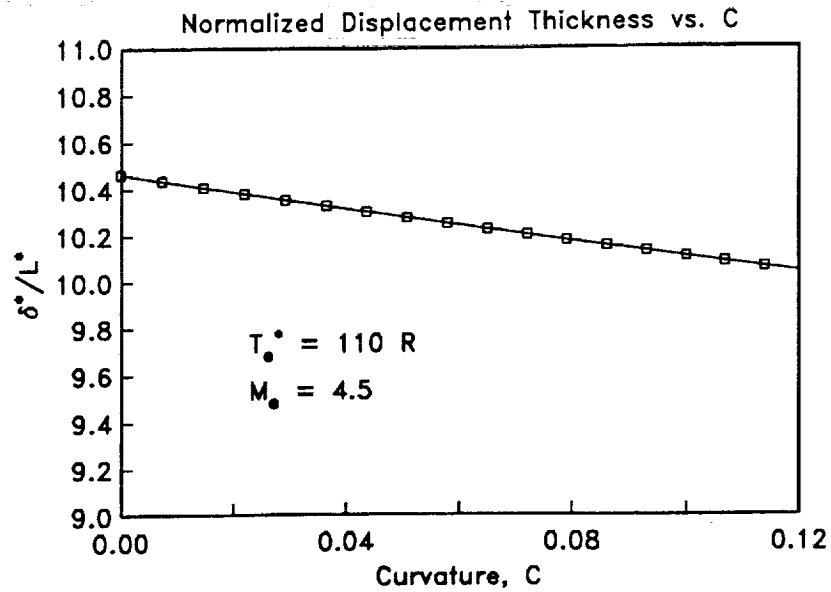
4) Variation of relative displacement thickness δ^*/L^* with curvature C at Mach 4.5 (wind tunnel conditions).
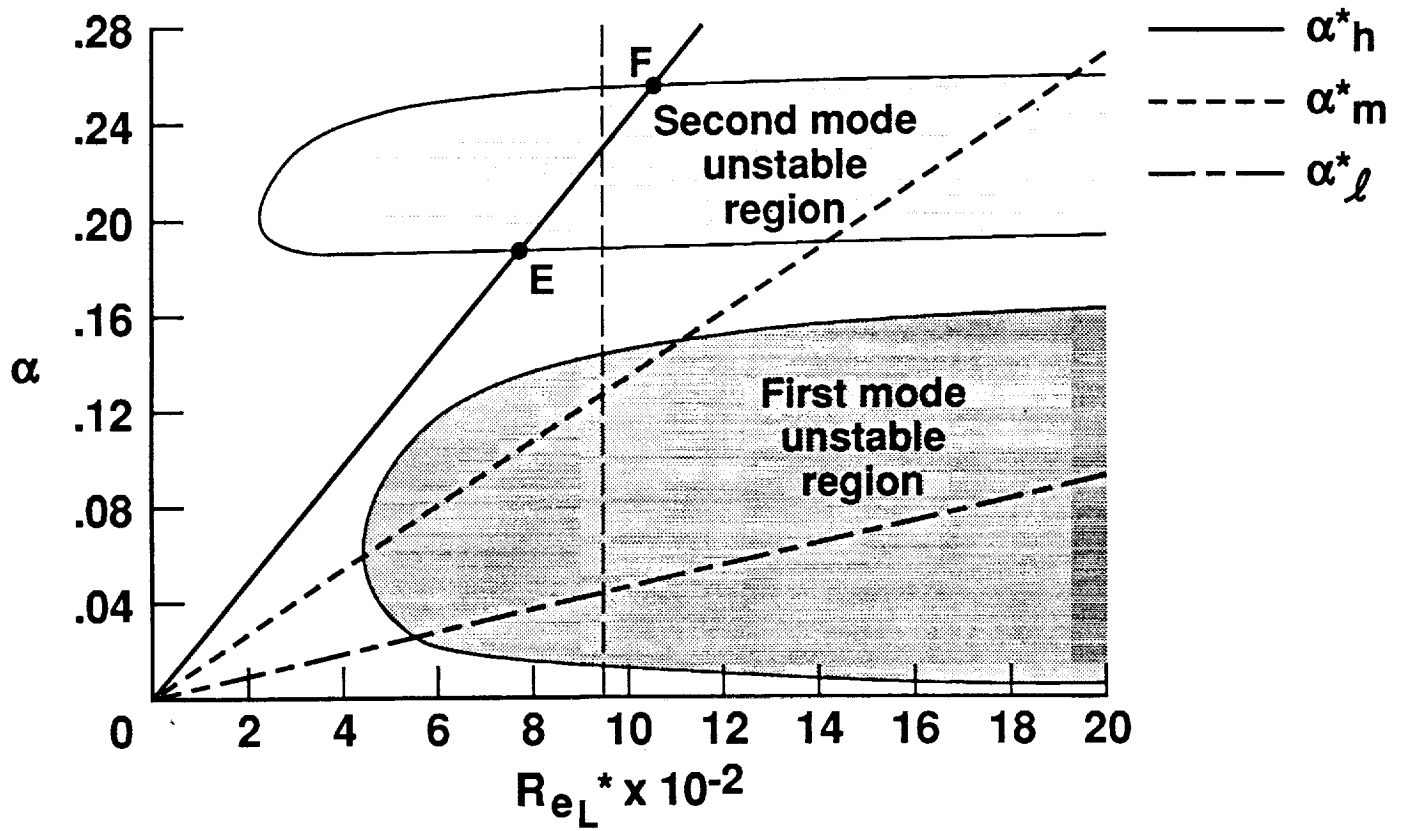
5) Neutral-stability curves for first and second-mode disturbances at Mach 4.5, with rays of constant dimensional wavenumber: _____ α_h^*; __ __ α_m^*; _ __ _ α_l^* (adapted from L. Mack [31], with permission.)
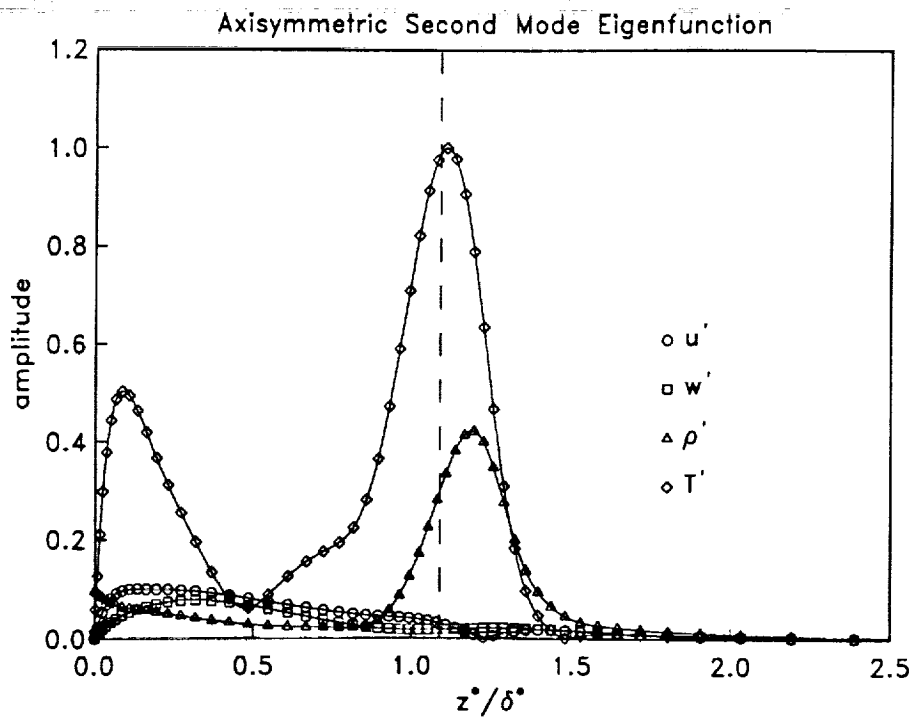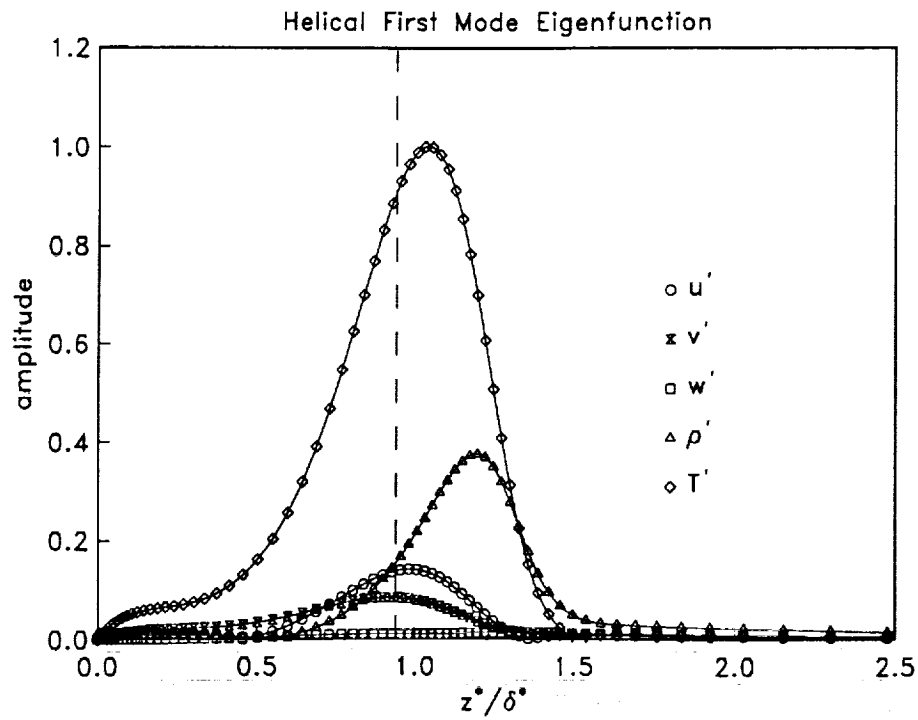
6) Eigenfunction components of a) a helical first-mode disturbance, and b) an axisymmetric second-mode disturbance at Mach 4.5.
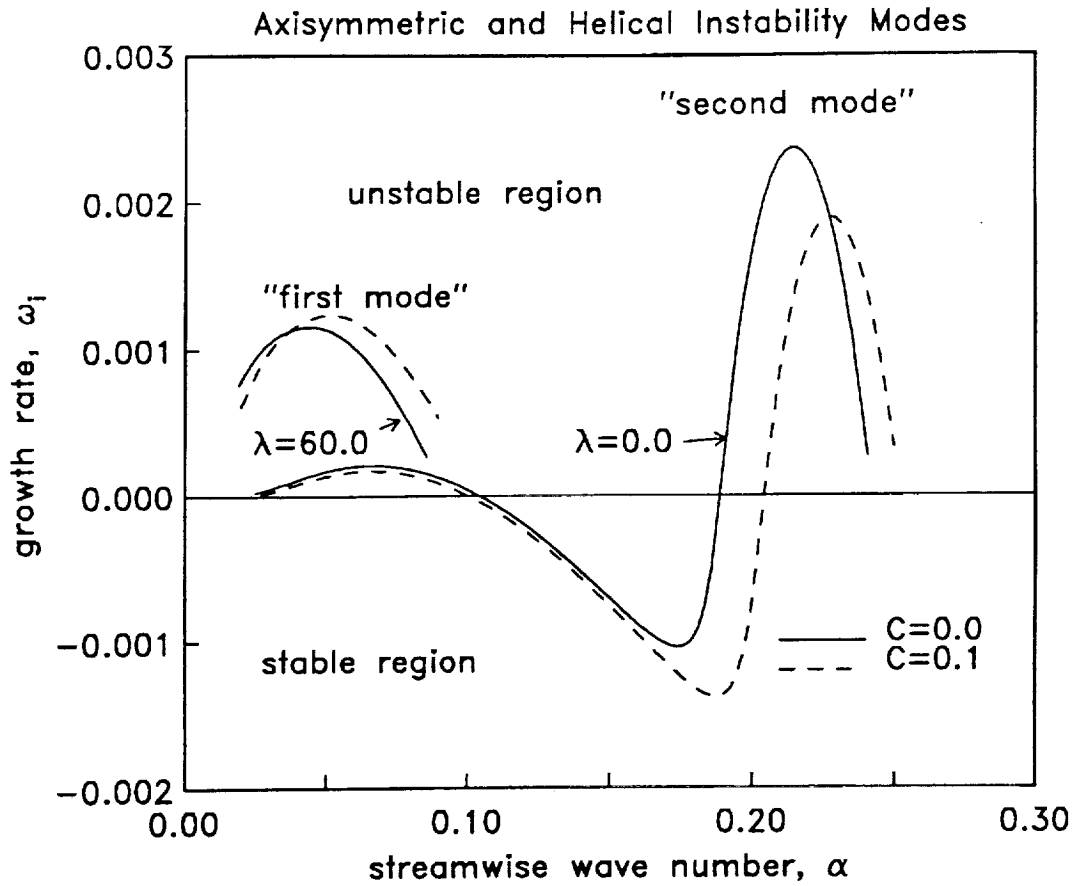
7)   Influence of moderate transverse curvature on axisymmetric first and second-mode disturbances at Mach 4.5.

Temporal Growth Rate vs. Transverse Curvature

$\alpha = 0.20$

Growth Rate, ω_i

Transverse Curvature, C

Temporal Growth Rate vs. Transverse Curvature

combined
indirect
direct

$\alpha = 0.22$

Growth Rate, ω_i

Transverse Curvature, C
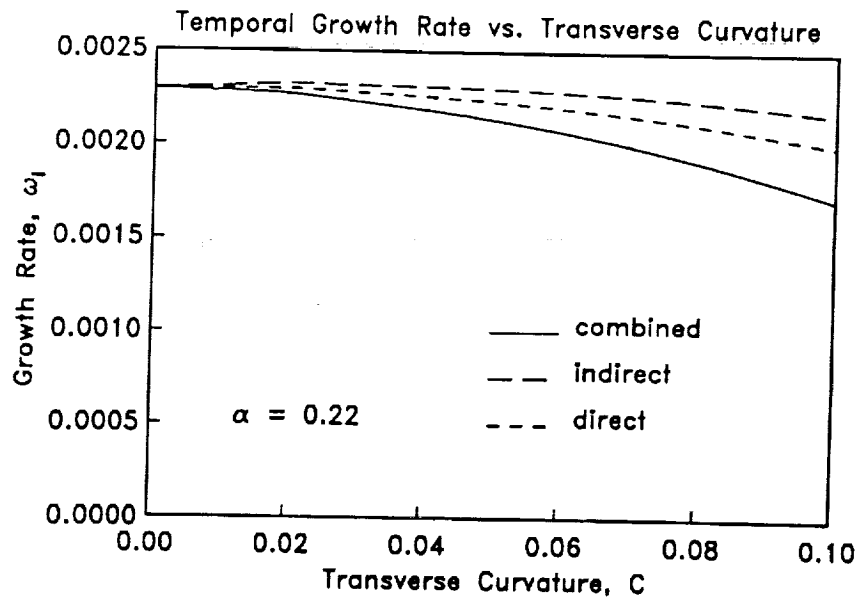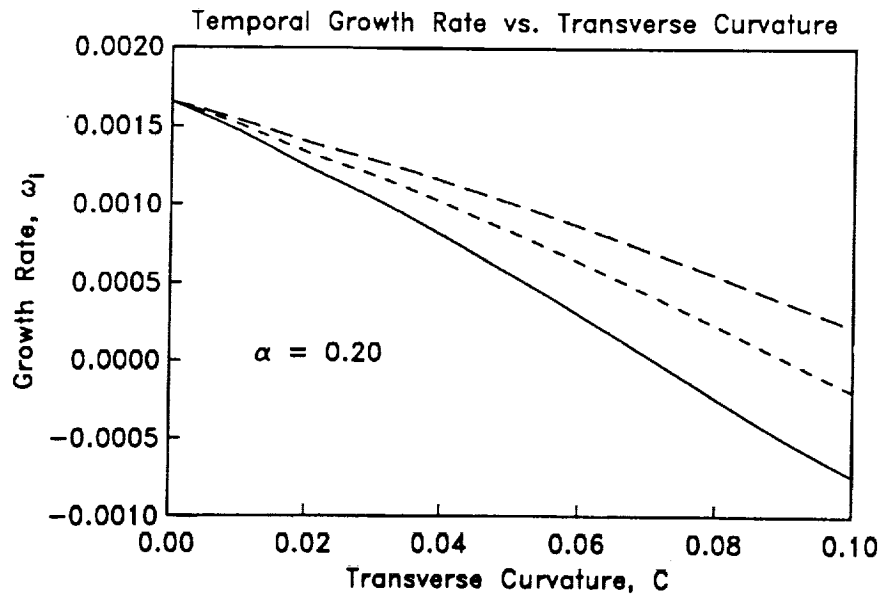
8)   Influence of increasing transverse curvature C on second-mode disturbances at Mach 4.5, for wavenumbers: a) α=0.20; and b) α=0.22
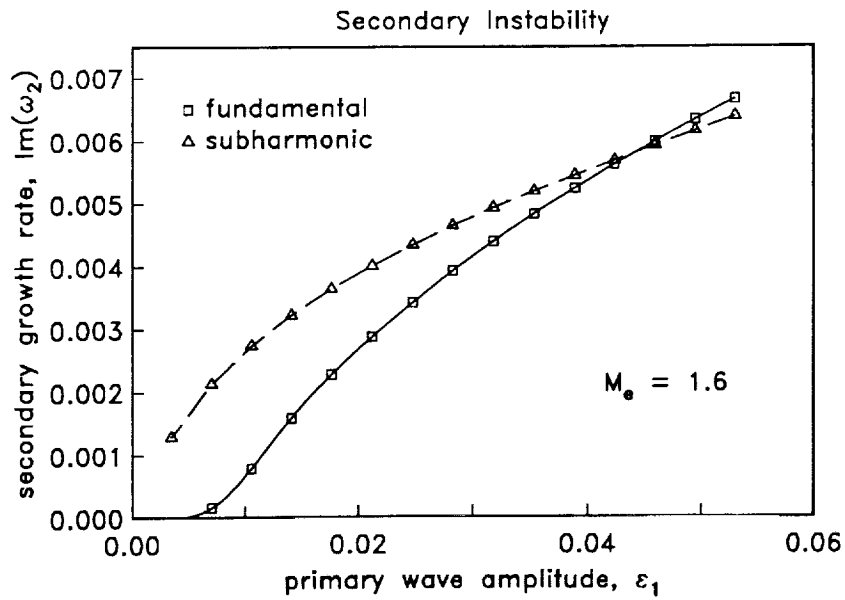
9)   Growth rates of a secondary disturbances of fundamental and subharmonic types as a functions of primary disturbance amplitude at Mach 1.6.
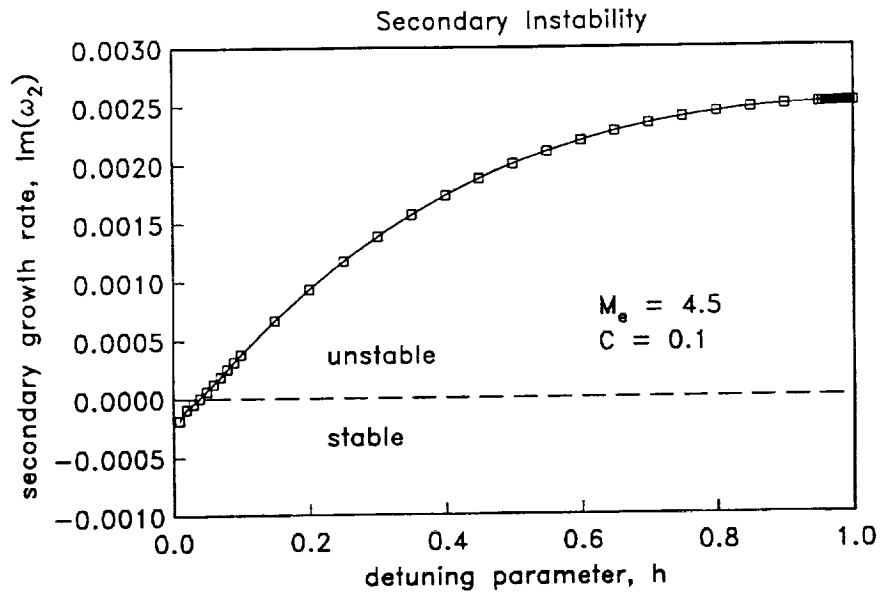
10)   Influence of detuning parameter h on secondary disturbance growth rate at Mach 4.5.

Subharmonic Secondary Instability
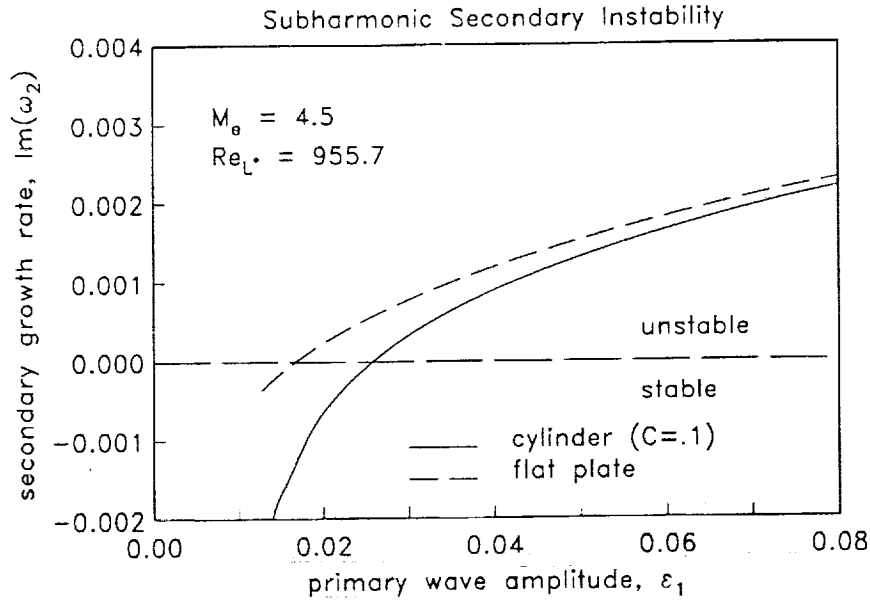
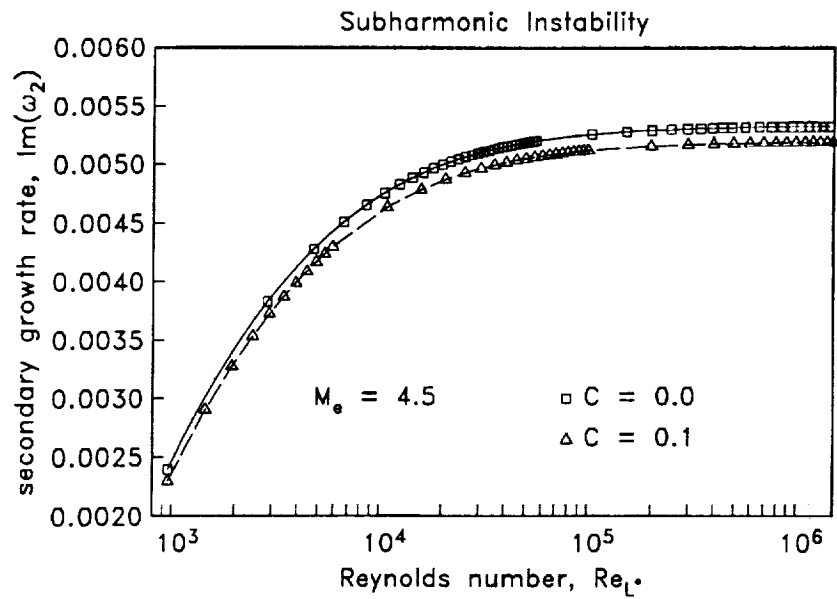11) Growth rate of a subharmonic secondary disturbance as a function of primary disturbance amplitude at Mach 4.5.

Temporal Growth Rate vs. Transverse Curvature
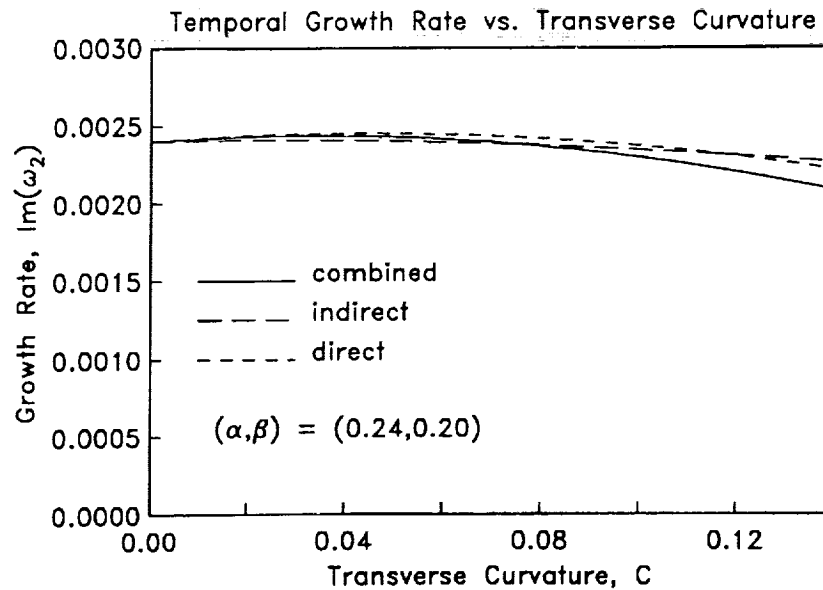
12) Influence of increasing transverse curvature C on subharmonic secondary instability at Mach 4.5.

Subharmonic Secondary Eigenfunction
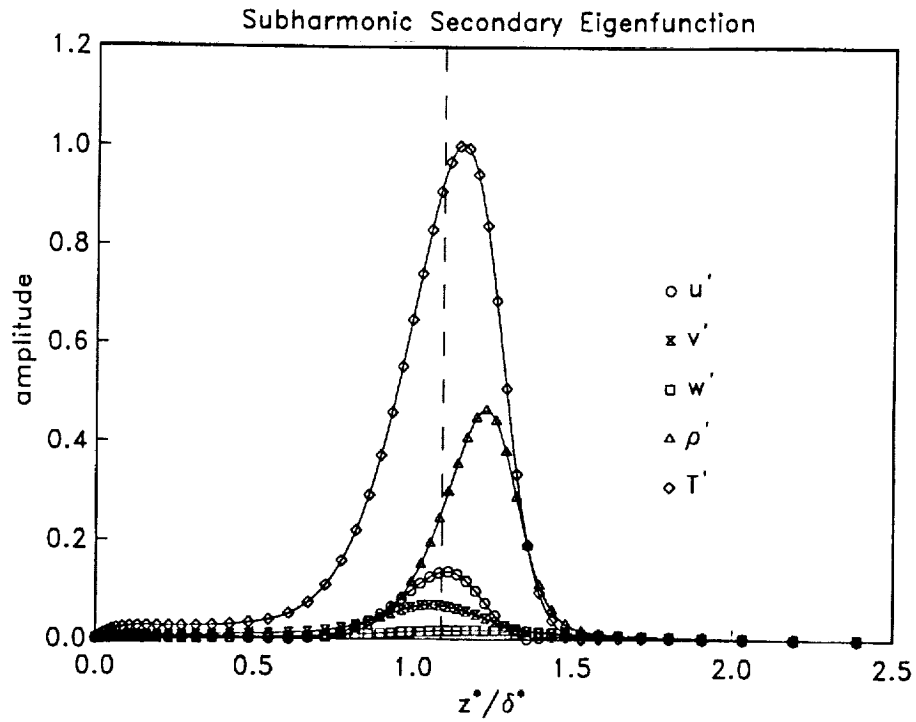
13) Eigenfunction components of a subharmonic-type secondary disturbance at Mach 4.5.

Subharmonic Instability

14) Influence of increasing Reynolds number on a subharmonic secondary instability mechanism at Mach 4.5.

Temporal Growth of Selected Harmonics
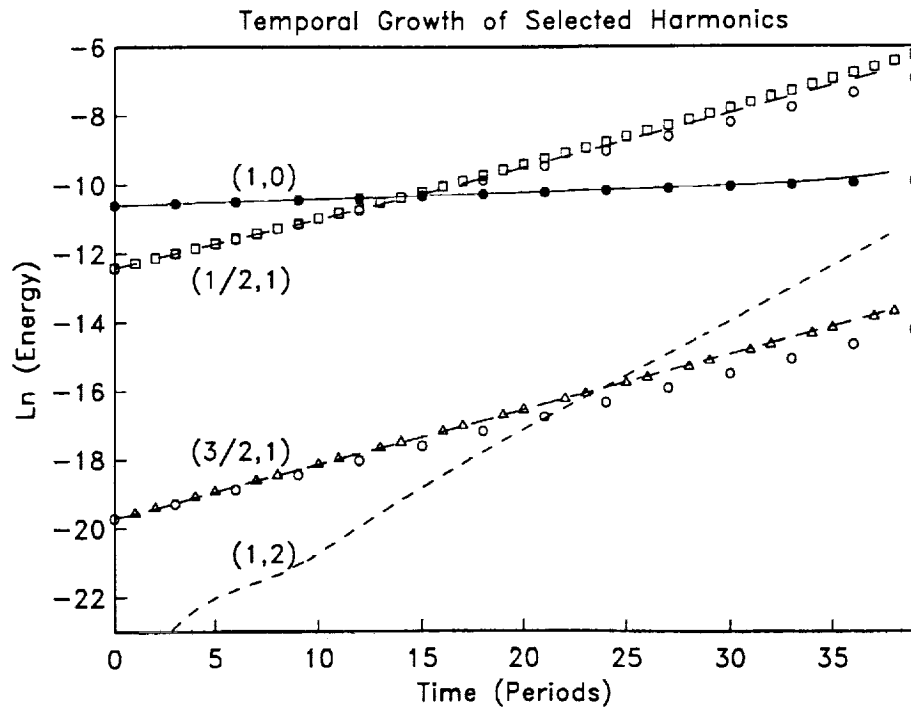
15) Temporal growth of the energy content of selected harmonics: ----- direct simulation, primary; - - - direct simulation, secondary; ● theory, primary; O theory, secondary; Δ theory modified according to eqs. (20); □ growth at the rate $Im(\omega_1+\omega_2)$.
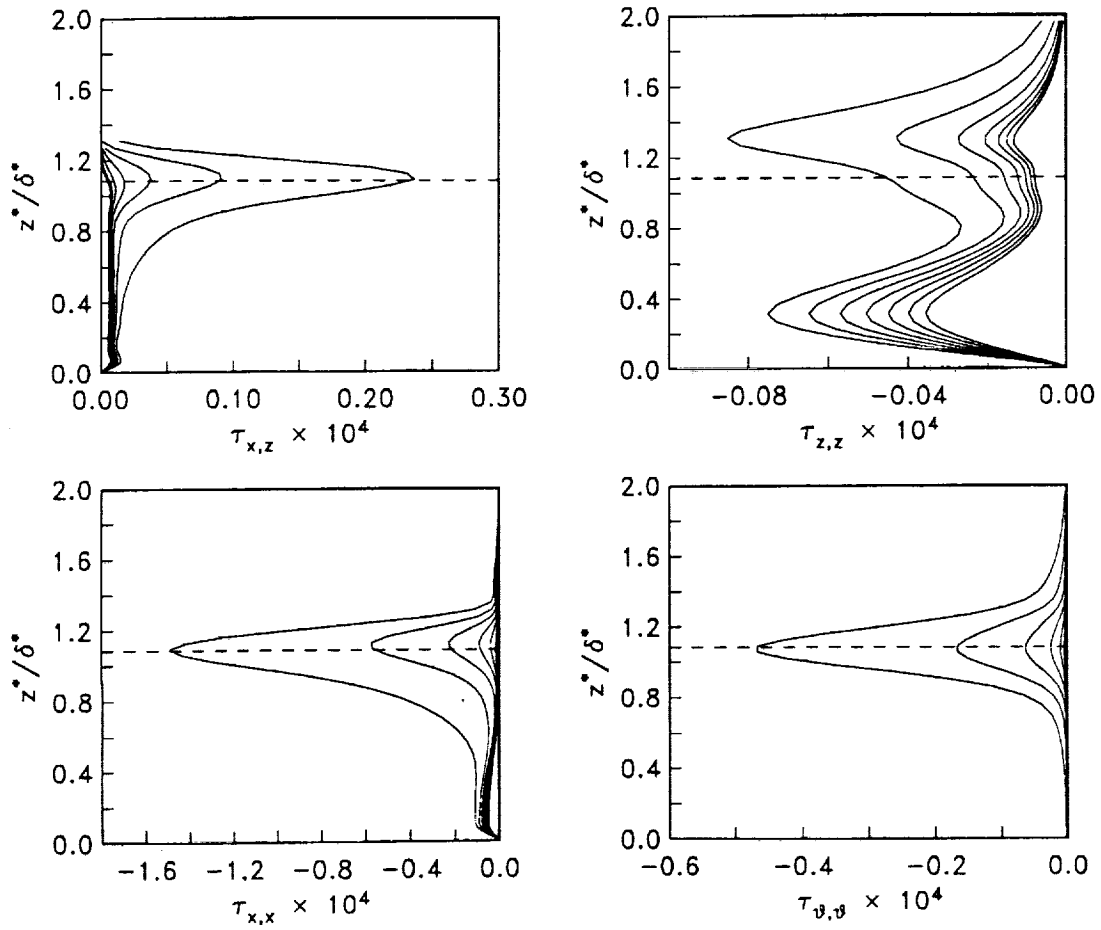
Temporal Evolution of Mode (1,0)
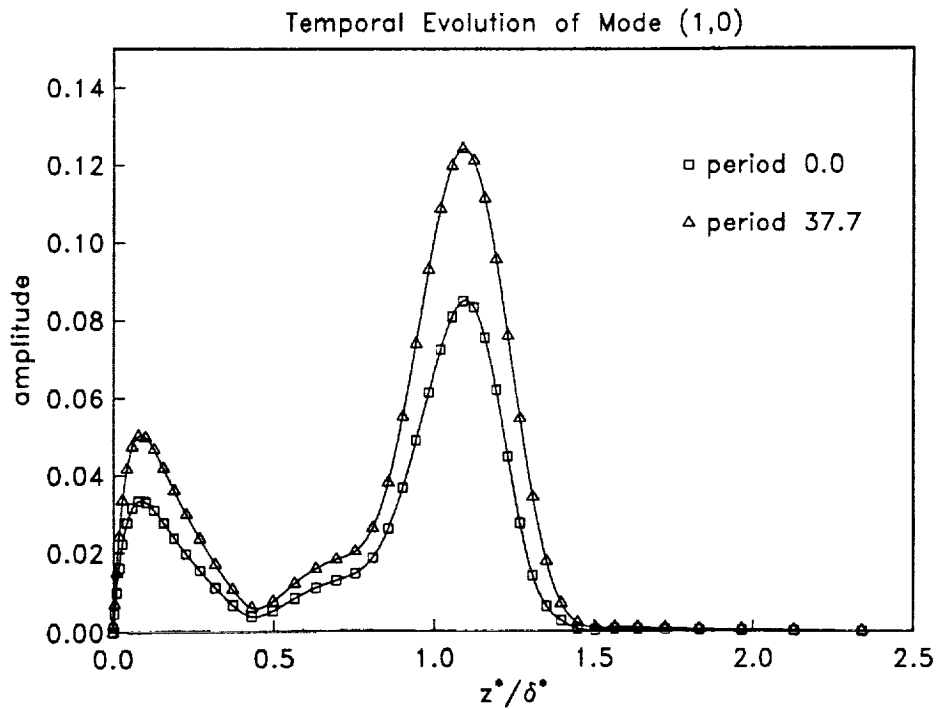
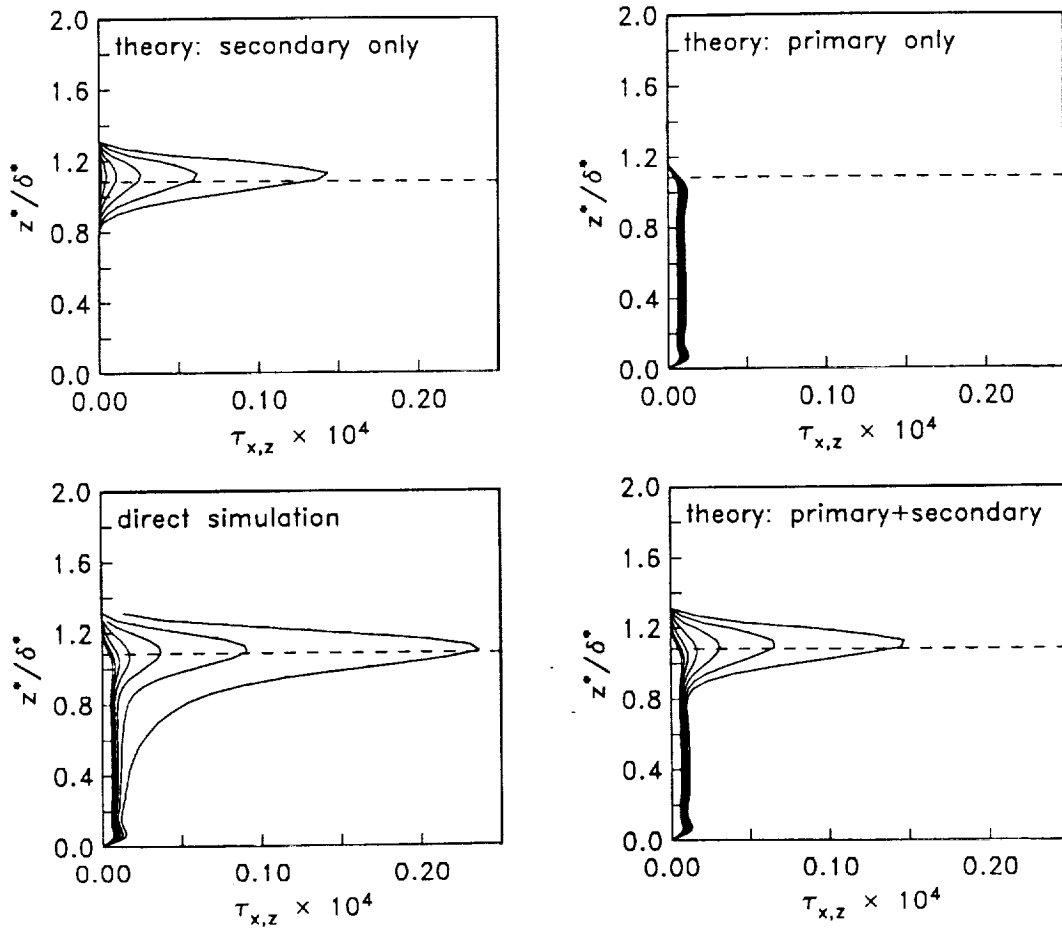16) Evolution of the temperature component of the fundamental (1,0) mode.
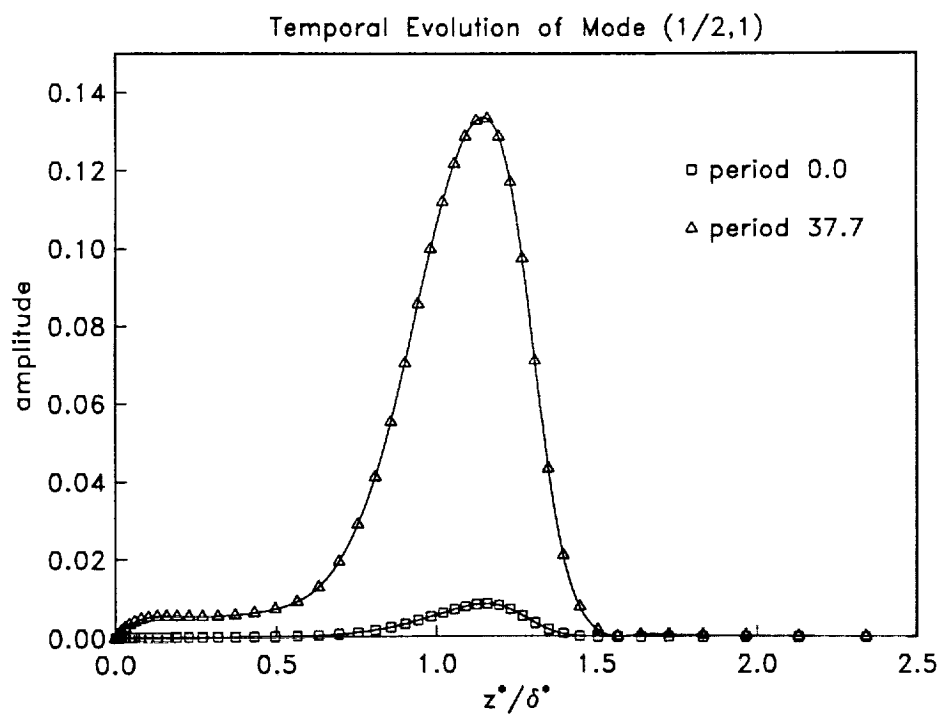
17)   Evolution of the temperature component of the (1/2,1) harmonic mode.
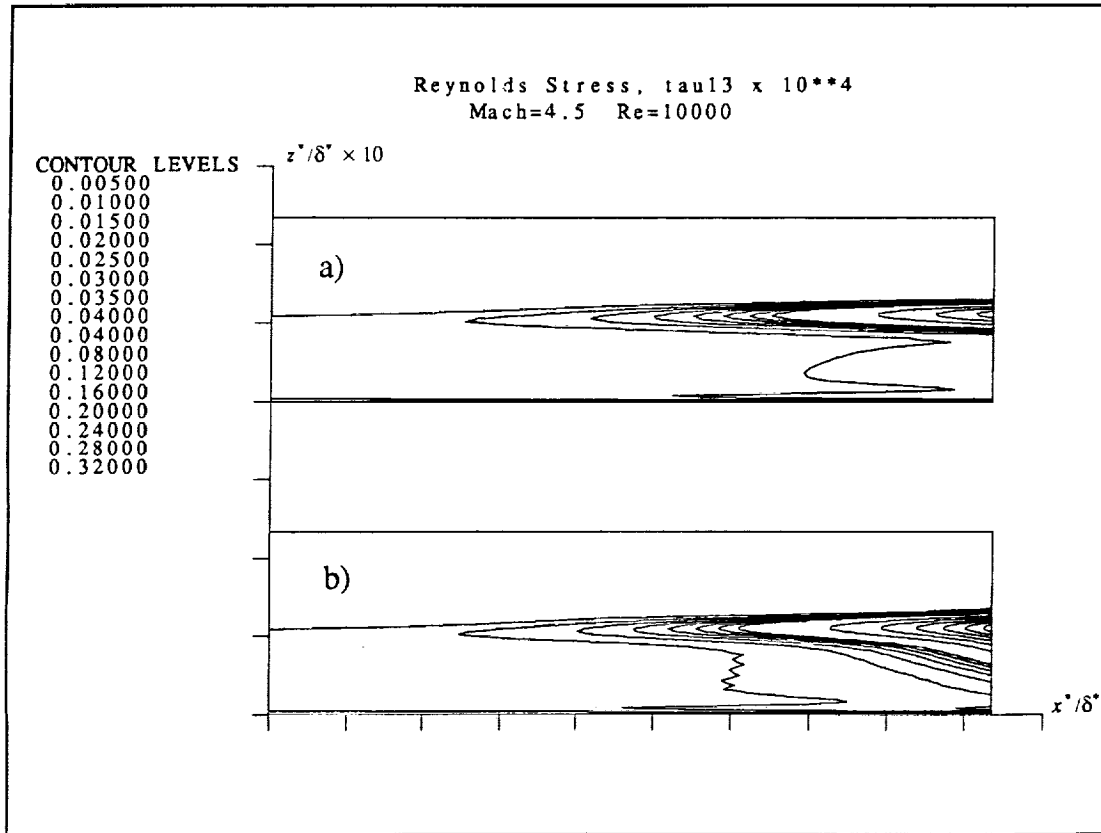
Averaged Reynolds Stresses
(Six Period Intervals)

18) Radial distribution of spatially-averaged Reynolds stresses at selected time intervals.
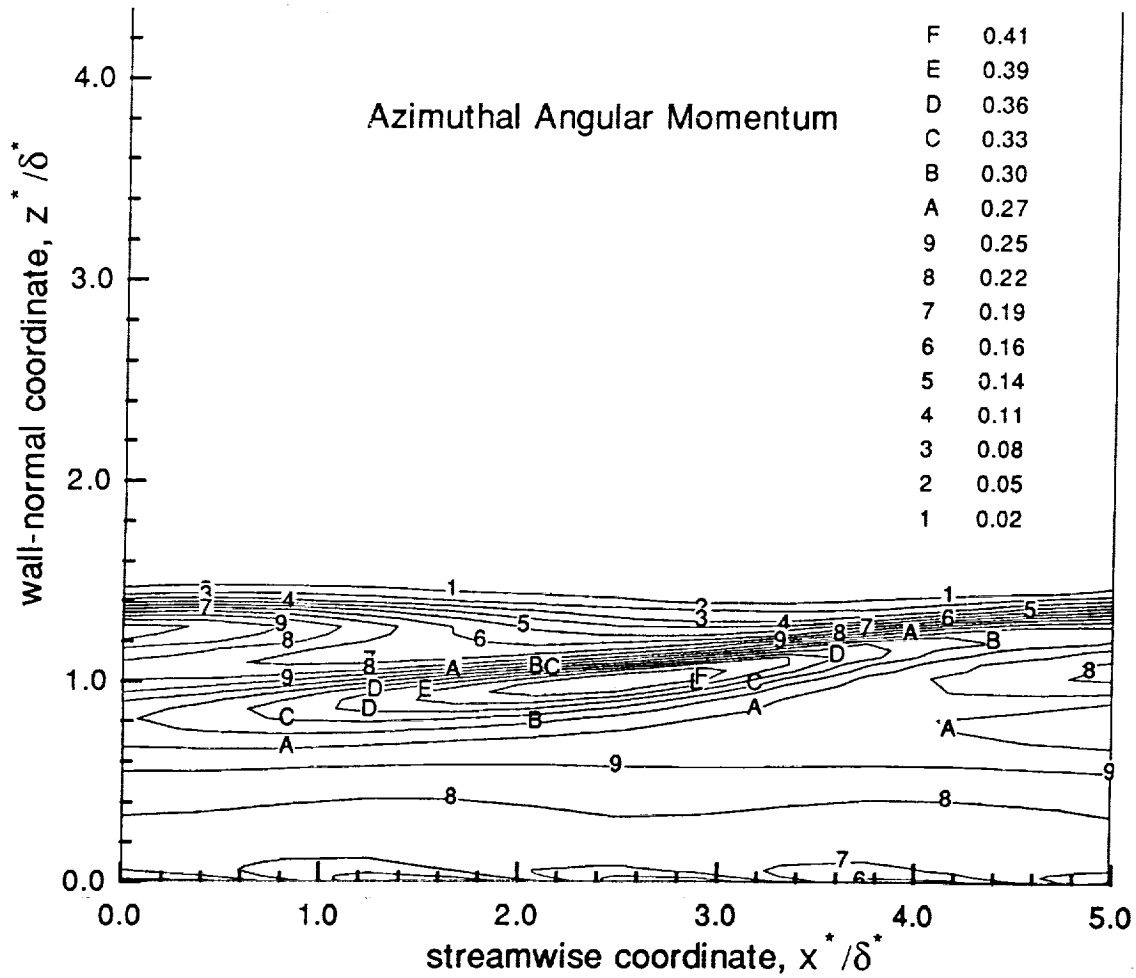
Averaged Reynolds Stresses
(Six Period Intervals)

19) Comparison between direct numerical simulation and secondary instability theory for the $\tau_{x,z}$ Reynolds stress.

Reynolds Stress, tau13 x 10**4
Mach=4.5   Re=10000

CONTOUR LEVELS
0.00500
0.01000
0.01500
0.02000
0.02500
0.03000
0.03500
0.04000
0.04000
0.08000
0.12000
0.16000
0.20000
0.24000
0.28000
0.32000

$z^*/\delta^* \times 10$

a)

b)

x^*/δ^*

20)   Approximate spatial evolution of the $\tau_{x,z}$ Reynolds stress based on Gaster's transformation: a) secondary instability theory; b) direct numerical simulation.
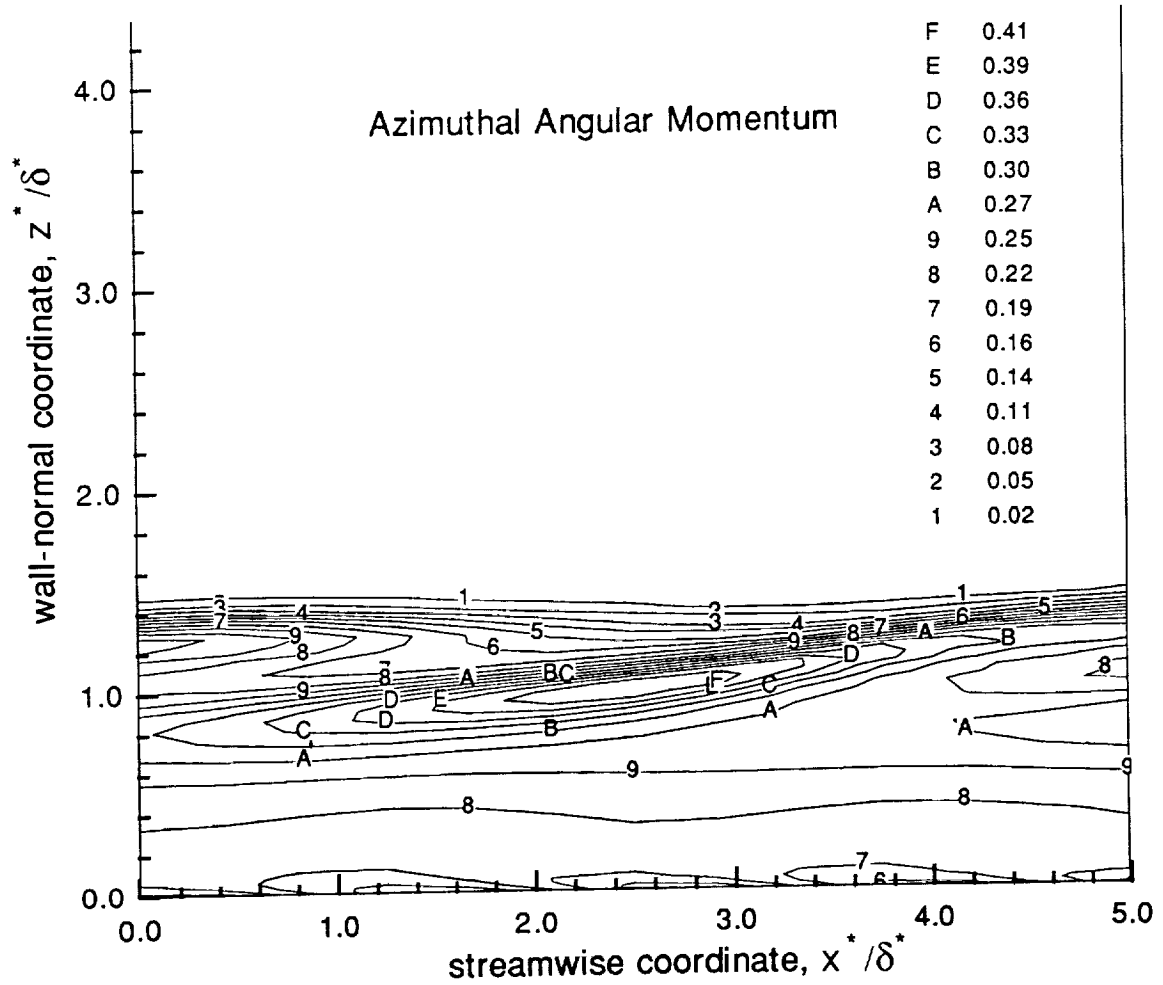
21) Comparison of a) iso-vorticity contours and b) contours of constant angular momentum in the $\theta=0$ x-z plane.

21) Comparison of a) iso-vorticity contours and b) contours of constant angular momentum in the θ=0 *x−z* plane.

NASA

National Aeronautics and
Space Administration

Report Documentation Page

1. Report No. NASA CR-187538 ICASE Report No. 91-30	2. Government Accession No.	3. Recipient's Catalog No.
4. Title and Subtitle ON THE NONLINEAR STABILITY OF A HIGH-SPEED, AXISYMMETRIC BOUNDARY LAYER		5. Report Date March 1991
		6. Performing Organization Code
7. Author(s) C. David Pruett Lian L. Ng Gordon Erlebacher		8. Performing Organization Report No. 91-30
		10. Work Unit No. 505-90-52-01
9. Performing Organization Name and Address Institute for Computer Applications in Science and Engineering Mail Stop 132C, NASA Langley Research Center Hampton, VA 23665-5225		11. Contract or Grant No. NAS1-18605
12. Sponsoring Agency Name and Address National Aeronautics and Space Administration Langley Research Center Hampton, VA 23665-5225		13. Type of Report and Period Covered Contractor Report
		14. Sponsoring Agency Code

16. Abstract

    The stability of a high-speed, axisymmetric boundary layer is investigated using secondary instability theory and direct numerical simulation. Parametric studies based on temporal secondary instability theory identify subharmonic secondary instability as a likely path to transition on a cylinder at Mach 4.5. The theoretical predictions are validated by direct numerical simulation of temporally-evolving primary and secondary disturbances in an axisymmetric boundary-layer flow. At small amplitudes of the secondary disturbance, predicted growth rates agree to several significant digits with values obtained from the spectrally-accurate solution of the compressible Navier-Stokes equations. Qualitative agreement persists to large amplitudes of the secondary disturbance. Moderate transverse curvature is shown to significantly affect the growth rate of axisymmetric "second mode" disturbances, the likely candidates of primary instability. The influence of curvature on secondary instability is largely indirect but most probably significant, through modulation of the primary disturbance amplitude. Subharmonic secondary instability is shown to be predominantly inviscid in nature, and to account for spikes in the Reynolds stress components at or near the critical layer.

17. Key Words (Suggested by Author(s)) transition, stability, secondary instability, cylinder, nonlinear, direct numerical simulation, compressible, Navier-Stokes	18. Distribution Statement 02 - Aerodynamics 34 - Fluid Mechanics and Heat Transfer Unclassified - Unlimited	
19. Security Classif. (of this report) Unclassified	20. Security Classif. (of this page) Unclassified	21. No. of pages 46 22. Price A03